An efficient hydrogenation catalytic model hosted in a stable hyper-crosslinked porous-organic-polymer: from fatty acid to bio-based alkane diesel synthesis

Chitra Sarkar, Subhash Chandra, Duy Quang Dao, Lee Jihyeon, Tran Khanh Ngoc Nguyen, Ramana Singuru, An Kwangjin, Nguyen Dang, Quyet Van, Prince Nana Amaniampong, et al.

ARTICLE

Efficient Hydrogenation Catalytic Model Hosted in Stable Hyper-crosslinked Porous-Organic-Polymer: From Fatty Acids to Bio-based Alkanes Diesel Synthesis

Received 00th January 20xx,
Accepted 00th January 20xx

DOI: 10.1039/x0xx00000x

Chitra Sarkar,[#,a] Subhash Chandra Shit,[#,a] Duy Quang Dao,[#,b] Jihyeon Lee,[c] Ngoc Han Tran,[d] Ramana Singuru,[a] Kwangjin An,[c] Nguyen Dang Nam,[b] Quyet Van Le,[b] Prince Nana Amaniampong,[e] Asmaa Drif,[f] Francois Jerome,[e,f] Pham Thanh Huyen,[g] Thi To Nga Phan,[g] Dai-Viet N. Vo,[h] Nguyen Thanh Binh,[i] Quang Thang Trinh*[,b,j] Matthew P. Sherburne*[,k,l] and John Mondal*[,a]

Correspondence to: qttrinh@ntu.edu.sg; trinhquangthang@duytan.edu.vn (Q.T.T)
mpsherb@berkeley.edu (M.P.S); johncuchem@gmail.com (J.M)

In this study, Pd-based catalytic model hosted over nitrogen enriched fibrous Porous-Organic-Polymer (POP) is established to execute hydrodeoxygenation of various vegetable oils in producing potential large-scale renewable diesel. Here we report a cost effective synthesis strategy of a new microporous hypercrosslinked POP through the $FeCl_3$ assisted Friedel-Crafts alkylation reaction, followed by fabrication of Pd^0-NPs (2-3 nm) with solid gas phase hydrogenation route to deliver a novel catalytic system. This catalyst (called Pd@PPN) exhibits versatile catalytic performance for different types of vegetable oils including palm oil, soybean oil, sunflower oil and rapeseed oil to furnish long chain diesel range alkanes. The catalyst is comprehensively characterized by various spectroscopic tools and shows high stability during five runs of recycling without the leaching of Pd occuring. Our results further reveal that direct decarbonylation (DCN) pathway of fatty acid to produce alkanes with one carbon less is the dominated mechanism. At optimized conditions, using stearic acid to represent the long linear carboxylic acids in the vegetable oils, up to 90 % conversion with 83 % selectivity of C17-alkane has been achieved on our fabricated catalyst. Density functional theory (DFT) calculations are performed to provide insights into the electronic properties of the catalyst, the mechanistic reaction pathway, the crucial role of catalyst surface and the product selectivity trend. The strong interaction between corrugated polymer-frame-structure and the Pd-NPs suggests there is the presence of high density step sites on the fabricated Pd-NP anchored within the cage of polymer structure. DFT calcualtions also reveal the strong promotional effect of step sites and charge transfer in facilitating rate-limiting steps during the decarbonylation (DCN) pathway and removal of strongly bound intermediates formed during the process, therefore explain the high activity of the fabricated Pd@PPN catayst for the hydrodeoxygenation (HDO) conversion to produce bio-based alkanes diesel.

[a] Catalysis & Fine Chemicals Division, CSIR-Indian Institute of Chemical Technology, Uppal Road, Hyderabad-500007, India.
[b] Institute of Research and Development, Duy Tan University, 03 Quang Trung, Danang 550000, Viet Nam.
[c] School of Energy & Chemical Engineering, Ulsan National Institute of Science and Technology (UNIST), Ulsan 689-798, Korea.
[d] Department of Aquatic Sciences and Assessment, Swedish University of Agricultural Sciences SLU, Box 7050, SE-750 07 Uppsala, Sweden.
[e] CNRS Research federation INCREASE, 1 rue Marcel Doré, TSA 41105, 86073 Poitiers, France.
[f] Institut de Chimie des Milieux et Matériaux de Poitiers (IC2MP), Université de Poitiers, CNRS, 1 rue Marcel Doré, TSA 41105, 86073 Poitiers, France.
[g] School of Chemical Engineering, Hanoi University of Science and Technology (HUST), 1 Dai Co Viet, Hanoi, Viet Nam
[h] Center of Excellence for Green Energy and Environmental Nanomaterials (CE@GrEEN), Nguyen Tat Thanh University, 300A Nguyen Tat Thanh, District 4, Ho Chi Minh City 755414, Vietnam
[i] Faculty of Chemistry, VNU University of Science, Vietnam National University, Hanoi, 19 Le Thanh Tong, Hanoi, Vietnam
[j] Cambridge Centre for Advanced Research and Education in Singapore (CARES), 1 Create Way, Singapore 138602.
[k] Materials Science and Engineering Department, University of California, Berkeley, Berkeley, California 94720, United States of America.
[l] Berkeley Educational Alliance for Research in Singapore (BEARS),1 CREATE Way, 138602 Singapore

# C.S., S.C.S. and D.Q.D. are equally contributed

Electronic Supplementary Information (ESI) available: [details of any supplementary information available should be included here]. See DOI: 10.1039/x0xx00000x

Introduction

In recent decades, the use of renewable energy resources such as biodiesel has increasingly gained attention owing to its ability to reduce CO_2 emission and other greenhouse gases from the consumption of fossil fuels.[1-3] Various alternative energy sources like solar, wind, and nuclear energy are developing nowadays, however the utility of solar, wind energy have the severe limitation by the surrounding environment and nuclear energy application suffers from drawbacks like residue deposition and radiation pollution.[4] Among renewable resources, biomass-based fuels are considered as potential alternative to conventional fossil derived liquid fuels.[5-8] The main component of natural oils and fats are triglycerides and free fatty acids comprised of longer linear chain hydrocarbon in the range of C4-C24.[9] The non-edible oils derived from jatropha, neem, karanja trees as well as waste cooking oil which are the main feedstock of fatty acids are readily available in developing

countries and economically viable compare to edible oil. The afore-mentioned renewable feedstock are the most desirable sources for the future transportation fuel due to their high energy density as well as structural similarity with fossil fuels.[4] Unfortunately, high viscosity and low volatility of natural oils suffer the serious disadvantage of using directly to the engine such as injector coking, carbon deposits and lubricant thickening.[10, 11] Researchers are now struggling to develop the sustainable method to upgrade biodiesel from these renewable feedstock.[12, 13] To overcome the drawback of direct applications of natural oils to the engine, oxygen content reduction from the fuel would readily ameliorate fuel stability, thus allowing to create better utilisation potential.[14] Cracking of triglycerides performed by zeolite would reduce the oxygen moieties, but create significant portion of carbon lose, responsible for energy loss.[15] The homogeneous base catalysis of fatty acids lead to the formation of fatty acid methyl esters (FAME) through transesterification, but FAME are considered as "drop in" fuel solution compared to conventional fuels due to their low energy density, higher cloud and smoke point along with poor cold flow properties.[16] Contrarily, high oxygen content of FAME make it unsuitable for diesel engine and during the process the situation became out of control by the deactivation of the catalyst through the saponification reaction of free fatty acids.[11] Hence, deoxygenation of the fatty acid and triglycerides by removing oxygen content in the form of CO, CO_2, and H_2O is the best proof of concept reaction to upgrade non-edible oil and waste cooking oil in biofuel industry, although the atom economy of the reaction is off. First generation biodiesel is produced directly from food crops (i.e. vegetable oil) and contains fatty acid methyl esters (FAMEs) and its hydrocarbons.[17] However, the first generation biodiesels shows severe drawbacks, such as high oxygen and acidity content, which hinders its ability to be utilised for large-scale applications compared to fossil fuels.[16, 18-20] To overcome these limitations, second-generation bio-fuels which are basically free of oxygen and compatible with petroleum diesel are being developed. Green biodiesel has notable features, such as higher heating value, oxidation stability, energy density, and cetane number comparable to conventional biodiesel.[21-23] In general, the production of green biodiesel from fatty acids is known to involve various deoxygenation methods,[24] such as decarboxylation (DCX), decarbonylation (DCN) and hydrodeoxygenation (HDO). These pathways have been reported to be incredibly efficient deoxygenation methods for the removal of oxygen moieties from oxygen containing compounds to form alkane and hydrogen (H_2).[17-21]

In nature, two types of fatty acids are available and exist as saturated and unsaturated acids. The number of carbon atoms in the fatty acid chains often ranges substantially from C8 to C24, but C12, C16, and C18 fatty acids are the most abundant in nature.[25-27] Saha *et al.* reported silica supported Ir-ReO_x bimetallic catalyst for the HDO of waste cooking oil and vegetable oil to diesel range alkane with 79-85% yield efficacy.[28] In another study, Bhaumik and co-workers also introduced Ru nanoparticles decorated on new porous organic network which exhibited tremendous catalytic activity for direct HDO of long chain fatty acids to hydrocarbons.[29] A very efficient Ru-HAP catalyst for the HDO of various types of oils (Jatropha oil, Palm oil, Waste cooking oil) to their respective long chain alkane for biodiesel industry was developed by Guo *et al*.[30] Chen and co-workers introduced zeolite-supported ruthenium catalysts to execute HDO of biodiesel-related fatty acid methyl esters to diesel-range alkanes.[31] HDO of waste cooking oil was investigated by Zheng and co-workers over unsupported CoMoS catalysts but the activity decreased associated with the gradual loss of sulfur.[32] An important finding of cascade reaction of terpene limonene dehydrogenation and stearic acid HDO through *p*-cymene accompanying H_2 formation over Pd-Ni/HZSM-5 catalyst was recently reported by Zhao *et al*.[33] Although all recent works demonstrated high catalytic efficiency for green diesel production, classical issues such as sulphide leaching, catalyst deactivation and high-cost bimetallic catalyst remain unsolved and there is a need to develop catalysts with higher activity, selectivity and stability for more realistic applications.

Currently, Porous Organic Polymers (POPs) have garnered significant interest within the scientific fraternity in the area of interdisciplinary research in catalysis,[34] gas separation[35] and CO_2 capture.[36] Owing to their exceptionally large surface area and tuneable pore-size, the cross-linked 3D cage-like structure can easily accommodate metal or metal oxide nanoparticles as active centers.[37-39] The molecular connectivity and chemical environment of POP framework can be readily tuned and tailored by altering synthetic strategy and selection of various geometry and size of monomers. While monomers exhibit essential role in the structural design of POP, the interfacial interaction between monomer and metal nanoparticles enhances the stability of the structure and the catalytic activity.[39-41] In addition, our research group has developed a series of POP supported catalysts which exhibited great catalytic performance in biomass conversion, revealing structural benefits for hydrogen activation and easy mass transfer through the porous network.[42, 43] Such robust POP framework could be used as a platform to host Pd NPs with no aggregation and activate the nanoparticles by electron-donating interaction. The system proved to be suitable for hydrogenation of oils in water under mild conditions though inhibiting leaching and catalyst deactivation.

In this work, we designed and developed a cost-free scalable synthesis of nitrogen enriched Porous Organic Polymeric network (PPN) by one-pot $FeCl_3$ assisted Friedel-Crafts alkylation reaction of triphenylamine (TPA) monomer and α,α'-dibromo-*p*-xylene as cross-linkers. The active Pd@PPN catalyst with homogenous dispensability of Pd-NPs (~2-3 nm size) was prepared by simple solid phase H_2 reduction route at high temperature. The Pd@PPN catalyst has been employed for the deoxygenation of stearic acid using green solvent (H_2O) rather than organic solvents, which made the permanent footprint in the biofuel industry as the utilization of organic solvent not only requires separation processes but also creates environmental hazards.[30] This catalyst also showed versatile

catalytic performance over different types of vegetable oils to furnish long chain alkanes. We have achieved a nearly quantitative yield in comparison with the theoretical values for possible long-chain alkanes based on the weight of the converted oils. In order to elucidate reaction pathway, we conducted control experiments using model substrates as probe molecule involving hydrogenation-hydrodehydration and direct decarbonylation/decarboxylation steps. Density Functional Theory (DFT) calculations were employed to study the interaction between the Pd-NPs and the polymer structure, evaluate their electronic properties and to elucidate the high activity of our catalyst for the HDO conversion of long linear-chain carboxyl acid.

Methodology

Synthesis of triphenylamine based Porous Organic Polymer Network (PPN)

Porous Organic Polymer Network (PPN) has been synthesized *via* $FeCl_3$ assisted template free Friedel-Crafts alkylation of triphenylamine (TPA) in the presence of α,α'-dibromo-*p*-xylene follwing the previous literature report by Bhaumik *et.al*.[44] In a typical synthetic procedure, 100 mL oven dried round bottom flask was charged with TPA (245 mg, 1 mmol) and α,α'-dibromo-*p*-xylene (396 mg, 1.5 mmol) and throughly mixed together in 20 mL of anhydrous 1,2-dichloroethane (DCE) solvent. Anhydrous $FeCl_3$ (487 mg, 3 mmol) was then added and the mixture was continously stirred for additional 10 h at room temperature under N_2 atmosphere. The resulting mixture was further heated to reflux for another 14 h. After that, the reaction was cooled down to room temperatrure and the bluish-black precipitate was dipped into acetone, collected and washed with methanol by centrifugation. To remove iron completely from the polymer, the product was further washed with methanol for three days in a soxhlet apparatus. Finally, the bluish-black precipitate was dried in an oven at 100°C over night and designated as PPN.

Fabrication of Pd^0-NPs on the PPN

Ultrafine Pd-NPs with an average size of 2-3 nm were fabricated on the PPN by solid-phase high temperature hydrogenation route (Figure 1). In a typical synthesis, 200 mg of PPN was added to 100 mL dichloromethane solution of $Pd(OAc)_2$ (80 mg) and continued for stirring at 60 °C for 24 h. After cooling to room temperature, the dichloromethane solvent was removed using the rotary evaporator and the resulting brown precipitate was filtrated and washed thoroughly with dichloromethane and MeOH to wipe out all the unreacted Pd-precursor. The obtained solid was dried at 80 °C for 12 h to give an as-synthesized brown solid; the latter was treated in a stream of H_2/N_2 (10% H_2, 100 mL/min) at 200 °C for 4 h. The resulting black solid was isolated and designated as Pd@PPN. It is noted that due to this procedure, a certain amount of Pd precursor has been wiped out during the filtration and wash. Our future work will be dedicated to develop the metal nanoparticles encapsulated by Porous-Organic-Polymer with different metal loading following more efficient synthetic protocols. For example, the Deposition-Precipitation technique is more efficient for better metal loading, in which the deposition from a precursor solution is facilitated through a change of pH, temperature, or evaporation… so that metal compounds are formed with a low solubility. Then the precipitation on the support can be nicely achieved when the surface free energy of small nuclei is decreased or the precipitate is stabilized through the introduction of the support.[45]

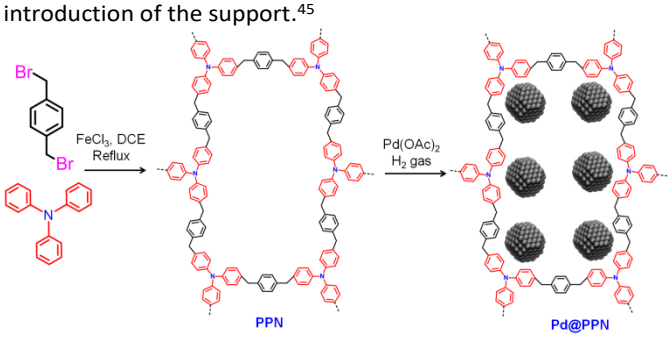

Figure 1: Schematic illustration for the synthesis of hyper-crosslinked nitrogen rich porous organic polymer network (PPN) and the corresponding Pd loaded polymer (Pd@PPN).

Catalytic Hydrogenation of Vegetable Oils over Pd@PPN Catalyst

Catalytic hydrogenations of various vegetable oils were conducted in a 100 mL Parr autoclave high-pressure reactor with a built-in pressure gauge setup having the range of 0-12 MPa and maximum temperature limit of 573 K. In a typical procedure, the pre-reduced Pd@PPN catalyst with the weight of 0.02 g was suspended into 50 mL of water and loaded into the reactor. The reactor was subsequently purged with H_2 gas for three times before the reaction to ensure the catalysts were still in their pre-reduced states, and then was charged with stearic acid (100 mg, 0.35 mmol) and 20 mL of water to initiate the reaction. The dissolved O_2 or air from the reactor was evacuated using a vacuum pump for 15 min at room temperature. During the reaction, H_2 pressure and the autoclave temperature were kept at 30 bar and 150 °C, respectively. The catalytic reaction was continued for the desired reaction time at a stirring speed of 1000 rpm. The reaction was monitored by sampling at regular time intervals, with analysis of the samples by an Agilent 6980 gas chromatograph (GC) equipped with a flame ionization detector (FID) and an SE-54 capillary column (30 mm × 0.32 mm × 1.0 µm) with a stationary phase GC. The products were quantified using n-Eicosane as an internal standard followed by comparison with known standards with a standard deviation less than 2%. After each catalytic reaction, the catalyst was isolated by simple centrifugation technique followed by washing with methanol several times and dried for overnight. After that, the catalyst was reduced again under solid-phase H_2 technique at 200°C for 4 h and further used for next catalytic test.

Computational details

To investigate the structure of the Pd NPs interacting with the PPN frame-structure and gain theoretical insights into the activities of the fabricated Pd-based catalyst for the HDO conversion of fatty acids,

we performed Density Functional Theory (DFT) calculations based on periodic boundary conditions and plane-wave pseudopotential implemented in the Vienna ab-initio simulation package (VASP), developed at the Fakultät für Physik of the Universität Wien.[46, 47] Projector augmented wave (PAW) method[48] employed with the Generalized Gradient Approximation (GGA) and a cut-off energy of 450 eV were used to describe the interaction between valence electrons and the ions. The optimized Becke88 functional (optB88) coupled with the non-local vdW-DF correlation (optB88-vdW) developed by Klimeš *et al.*[49-52] were used to correctly capture the van der Waals interaction between aromatic compounds and carboxylic acids with Pd surfaces for all DFT calculations. As reported in earlier studies, this level of theory was one the most appropriate to describe the interaction between aromatic compounds on transition metal surface and predict accurately the adsorption energies compare to experimental data.[52-54] Furthermore, since the van der Waals interaction between carboxylic acids and the transition metal surface is important,[55, 56] optB88-vdW functional is also a suitable choice for the investigation of carboxylic acids conversion on Pd@PPN catalyst. We have evaluated the performance of this chosen optB88-vdW functional in computing the adsorption energies for benzene and formic acid on several transition metals, and found the observed values are in very good agreement with experimental data, as are presented in Table T7 and Figure S11 of the SI. Transition states of the reactions occurred during the HDO conversion were located using the Climbing-Nudged Elastic Band (Cl-NEB) method.[57] Frequency calculations confirmed the nature of the transition states with only one imaginary vibrational frequency.

Theoretical investigation into the structure and electronic properties of Pd@PPN. In order to understand the structure of Pd NPs fabricated on the PPN frame-structure, DFT calculations using the optB88-vdW functional were conducted to study the interaction between one full unit monomer of the polymer structure (called *um*PPN molecule) and the Pd-NPs. The structure of the *um*PPN unit molecule is shown in Figure 2a and it is a very good representative molecule to study the interaction between Pd nano-particles and the Porous Polymer frame-structure since it contains both two monomer units for the polymer: TPA and p-xylene. To study the adsorption of *um*PPN on Pd NPs, we used a cluster approach to model the Pd particle with the size of 3 nm which was detected from experimental XRD (see Figure 3b) and TEM (see Figure 5d-f) analysis. Firstly, we built a structure representative for a 3 nm NPs with truncated octahedral shape involving 1289 Pd atoms in total (Fig. 2b). This cluster model was used for 3 nm size Ru particle in explaining the high activity of B5 step sites during the ammonia synthesis by Honkala *et al*.[58] and later was widely employed to study the activity of Pd NPs for different reactions such as methane activation,[59, 60] CO adsorption[61] and conversion.[62] However, due to the symmetric structure of this cluster and to make the calculations more efficient, we then used the simplified model including the upper half with only four top-most layers of the 3 nm truncated octahedral cluster NPs in the unit cell of 25 Å × 25 Å × 25 Å, now is called as the reduced cluster (Fig. 2c). The illustration of how to create the reduced cluster model from the full size model is presented in Figure S12, SI. The similar reduced-cluster model has also been conveniently used in a recent study by Zhou *et al.* to investigate the light-driven methane dry reforming on Cu-Ru nano-particles.[63] This reduced model has 332 Pd atoms (called Pd_{332} cluster) and only the Γ point was used to sample the Brillouin zone for DFT calculations on this model. All VASP calculations for this reduced Pd_{332} cluster model were performed with the invoking of the first-order Methfessel−Paxton smearing technique with a width of 0.1 eV, the electronic minimization was done using the mixture of the Davidson and RMM-DIIS algorithms and the conjugate-gradient algorithm was used to relax the ions into their instantaneous ground-state. To study the electronic properties of Pd@PPN material, the Bader charges of all the atoms were computed based on the charge density grid algorithm developed in Henkelman *et al.*[64, 65] Furthermore, the analysis of the Density of states (DOS) projected on the d-band for Pd atoms in different structures was also performed to understand the interaction between Pd and the porous polymer frame structure.

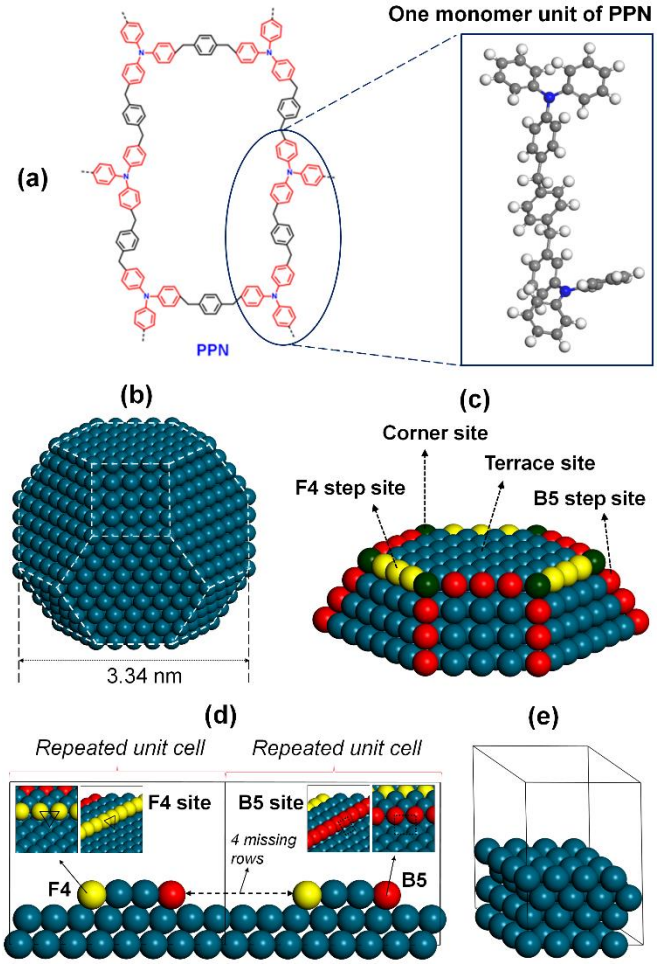

Figure 2: Models used for DFT investigation on the adsorption of TPA and the conversion of fatty acid on Pd NPs. (a) The structure of one full unit monomer of the polymer (called *um*PPN molecule) used to represent the Porous Polymer frame-structure**.** (b) Full cluster model of the 3 nm Pd NPs with truncated octahedral shape, including 1289 Pd atoms. (c) Reduced cluster model of 332 Pd atoms used to study the interaction of TPA with Pd NPs. (d) Model of p(4×8) Pd(111) slabs with 4 missing rows on the top layer. Different step sites (B5 and F4) are highlighted. (e) Model of terrace sites on p(4×4) Pd(111) slabs.

We have checked the adsorption energies of the TPA molecule on thicker clusters (including five layers) and they are almost identical to that on the four-layer cluster used herein (Figure S13. SI).[66] It is worthy to note that in our study, all VASP calculations were performed on CPU-mode only. Running VASP on Graphics Processing Unit (GPU) will accelerate the VASP electronic structure calculations significantly, as was documented in earlier reports[67-69] and with the release of modern graphics-processing unit architecture, VASP could run up to 10X faster compared to CPU-only systems, enabling usage of computationally more demanding and more accurate methods in the same time.

Investigation into the Hydrodeoxygenation (HDO) conversion of fatty acids on Pd@PPN catalyst. To evaluate the HDO reactions of fatty acids on Pd catalyst, butanoic acid was chosen as the model compound. As mentioned by Lu *et al*.[70], the computed gas-phase reaction energies for the decarbonylation (DCN) and decarboxylation (DCX) reactions of carboxylic acids to alkanes are converged and almost identical for reactants with carbon chain length larger than three. Evaluation of some electronics properties of C4, C5, C6 and C18 acids found that they gave similar results, justifying the appropriateness of using butanoic acid to represent stearic acid in our DFT calculations (see details in the SI). It should be mentioned here that for locating the transition states during the reaction of butanoic conversion by the Climbing-Nudged Elastic Band (Cl-NEB) method, typically a series of intermediate states (six to ten intermediate states) distributed along the initial reaction path connecting a reactant and a product state are simultaneously optimized while restricting atomic motions to hyperplanes perpendicular to the reaction path, making it not computationally efficient for large systems such as the reduce Pd_{332} cluster. Therefore, to make the computational evaluation more efficient in studying the HDO conversion of butanoic acid, we then used two other models to evaluate the activity of the fabricated Pd@PPN catalysts. The first model is the periodic three layers p(4×8) Pd(111) with 4 missing rows on the top layer (Fig. 2d). This model exposes two most popular step sites on it, the B5 and the F4 step sites, which are highlighted in Fig. 2d. Note that the B5 step sites are created at the intersection of a (111) and a (100) facet, and the F4 step sites are formed at the intersection between two (111) facets. This model also presents terrace sites next to those B5 and F4 steps sites, and is an excellent representative for the reduced Pd_{332} cluster in the Fig. 2c. The use of this model was very helpful and successfully applied for earlier theoretical studies in explaining the formation of nano-Co-islands and CO activation during the Fischer-Tropsch synthesis under realistic conditions[71, 72] and evaluating the activity of step sites in the conversion of methane,[2, 73] toluene[52] and amine-coupling reaction.[74, 75] We have also compared the adsorption energy and initial activation barriers of butanoic acid on B5 and F4 step sites of the reduce Pd_{332} cluster and on B5 and F4 step sites of the p(4x8) with 4 missing row model using the optB88-vdW functional, and the data showed that those obtained values are very close to each other (Table T9 and Fig S14, SI), justifying the appropriateness of using the p(4x8) with 4 missing row model to represent the Pd_{332} cluster in studying the reaction mechanism. The activity of the normal terrace sites which was dominated on larger-size particles[58] was evaluated using a slab model of *p*(4×4) Pd(111) surface (Fig. 2e). For all the slab models in this study, two topmost layers and the adsorbates were allowed to fully relaxed, while the atoms in the remaining bottom layers were fixed at their bulk optimized lattice constant of 3.94 Å.[7, 76] All the DFT calculations for the study of butanoic acid conversion on Pd terrace and step sites were also performed employing the optB88-vdW functional. The Brillouin zone was sampled with the value of a 3×3×1 Monkhorst–Pack grid for both the p(4×8) with 4 missing rows and the p(4×4) models. Repeated slabs in those two models were both separated by a vacuum of 20 Å above the topmost layer to minimize their interactions.

Results and discussion

Material Characterization

Herein, we defined a truly cost effective synthesis strategy of a new microporous hyper-crosslinked organic polymer networks PPN through the $FeCl_3$ assisted Friedel-Crafts alkylation reaction of triphenylamine (TPA) monomer and α,α'-dibromo-*p*-xylene.[44] The resulting material is rich in nitrogen content, which can be used as anchors to introduce palladium nanoparticles. The treatment of PPN with $Pd(OAc)_2$ followed by solid-phase reduction with 11% H_2 /N_2 mixture at high temperature gives the Pd@PPN materials.[77] The texture and chemical properties of as-synthesized PPN and Pd@PPN materials were characterized by wide angle X-ray scattering (WAXS), ^{13}C CP/MAS solid-state NMR spectroscopy, X-ray photoelectron spectroscopy (XPS), Transmission Electron Microscopy (TEM), high angle annular dark field scanning transmission electron microscopy (HAADF-STEM), energy-dispersive X-ray (EDX) elemental mapping, field emission scanning electron microscopy (FE-SEM) and nitrogen physisorption studies.

The elemental analysis confirmed that the PPN contains 83.65% C, 5.67% H and 4.21 wt.% of N, respectively. In strong contrast, Pd@PPN material contains 78.23% C, 5.12% H and 3.91 wt.% of N, respectively. Pd content in the Pd@PPN material is 0.459 mmol/g as measured by Inductive Couple Plasma Atomic Emission Spectroscopy (ICP-AES) technique. A little inconsequential difference in the experimental C and N content (%) from the corresponding theoretical values in the elemental (C, H, N) analysis could be explained by the accommodation of guest molecules in the porous channel of the host PPN, a very widespread phenomenon of porous materials.[78] The thermal stability of the as-synthesized PPN polymer investigated by thermogravimetric analysis (TGA) under N_2 atmosphere in the temperature range 25 to 800 °C is presented in the Figure S1, SI. At low-temperature region (< 100 °C), the negligible weight loss could be attributed to the evaporation of surface water and intercalated solvent molecules inside the polymeric cage. A sharp weight loss at 430 °C is observed, corresponds to the degradation of the organic framework. High thermal stability of this polymer could be attributed to the high hyperbranched cross-linking and the rigid polymeric networks in the molecular skeleton. FT-IR analysis of both as-synthesized PPN and Pd@PPN were conducted and the results are presented in the Figure S2, SI. The C-N stretching

of the tertiary amines in the organic backbone unit of the as-synthesized polymer reappeared as characteristic stretching vibrations of PPN material at 1278 cm^{-1}. The distinctive C-H out-of-plane bending vibrations of the *p*-disubstituted benzene rings is observed at 819 cm^{-1} while the bands at 1604 and 1494 cm^{-1} can be attributed to the strong stretching vibrations of the aromatic C=C bonds in the aromatic rings. The formation of the extended PPN network was additionally evidenced by the existence of characteristic Ph-CH_2 unit stretching modes at 2918 cm^{-1}. The FT-IR spectrum of the Pd@PPN material confirms that the structural bonding in the PPN framework remains intact after metal loading.

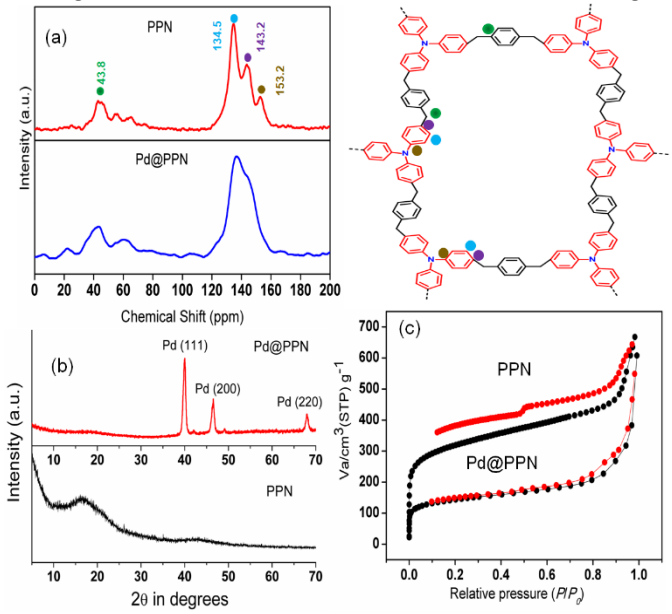

Figure 3: (a) ^{13}C CP/MAS solid state spectra, (b) Wide angle powder X-ray diffraction patterns; (c) N_2 adsorption/desorption isotherms.

The solid state ^{13}C CP/MAS NMR spectra of the as-synthesized PPN and Pd@PPN materials (Figure 3a) confirm the molecular connectivity of the structural integrities and chemical surroundings in the region of the different carbon nuclei. A weak signal at δ = 43.8 ppm in the spectrum of PPN is accorded to the carbon atom of methylene linker. The appearance of a strong signal at δ = 134.5 ppm confirms the non-substituted carbon atom of the aromatic rings, whereas the concomitant appearance of distinguishable signals centred at δ = 143.2 ppm and 153.2 ppm are accountable for the phenyl ring and N-substituted aromatic carbon atom of the triphenylamine unit. The Pd@PPN material exhibited chemical shifts quite analogous to the PPN, which unambiguously proved that the structural integrity of their rigid polymer backbone unit after palladium implantation is successfully retained, as proposed by Bhaumik and co-workers.[44] However, the peaks appeared in the MAS NMR spectrum of Pd@PPN with somewhat poor intensity and overlapped peaks indicated the complex nature of the metal loaded material. The wide-angle powder X-ray diffraction pattern (Fig. 3b) of as-synthesized PPN exhibited a weak broad diffraction peak at 2θ = 20.2°, which could be attributed to the π-stacking of the aromatic building blocks in small domains. This pattern shows the amorphous nature of our PPN material, obviously caused by the random polymerization of monomer unit upon heating conditions. Powder XRD pattern of Pd@PPN clearly showed the crystalline nature of the Pd-NPs loaded in the porous polymer. The characteristic Braggs angles at 2θ = 39.9°, 46.5°, 67.8° correspond to Pd (111), Pd (200), Pd (220) lattice planes, indicative for the face centred cubic (*fcc*) Pd-crystal. The result is in good agreement with previous literature (JCPDS no. 7440-05-3).[79] The Pd-NPs size was estimated to be of 3.0±0.5 nm, computed using the Debye-Scherrer equation for the highest intensity diffraction peak of the (111) crystalline lattice plane. The result is very consistent with the particle size obtained from TEM and HAADF-STEM analysis later.

To get the clear picture about the permanent porosity of the as-synthesized PPN and Pd@PPN materials, N_2 gas adsorption study were performed at 77 K. As shown in Fig. 3c, the N_2 adsorption-desorption isotherms of PPN exhibited high N_2 uptake at very low P/P_0 region, followed by gradual uptake with a very broad hysteresis loop at the high P/P_0 region. This typical type IV isotherm suggests the coexistence of micro and interparticle void spaces within the PPN framework. The broad hysteresis loop in the high-pressure region could be explained due to the swelling of polymeric network upon the gas adsorption, for which irreversible gas uptake can take place. However, flexible expansion of restricted access pores (closed pores) with the increase of P/P_0 could be also the key factor for the appearance of large hysteresis loop, in good agreement with the previous report by Bhaumik *et.al* in their nitrogen-rich porous organic polymer.[80] The Brunauer-Emmett-Teller (BET) surface areas and the total pore volumes were found to be (1165 m^2/g, 1.033 cm^3/g) and (679 m^2/g, 0.825 cm^3/g), for the PPN and Pd@PPN materials, respectively. The preservation of the isotherms shape for the N_2 adsorption/desorption with no hysteresis loop of Pd@PPN in comparison with the parent PPN material shows a considerable diminishment in the BET surface area with both partial pore occupancy and mass loading of Pd NPs. The Non-Local-Density-Functional-Theory (NLDFT) fitting of the adsorption branches model of both the PPN and Pd@PPN materials (Figure S3, SI) exhibited the narrow pore size distributions with the pores dimension predominately in the microporous range (1.54 nm & 1.28 nm).

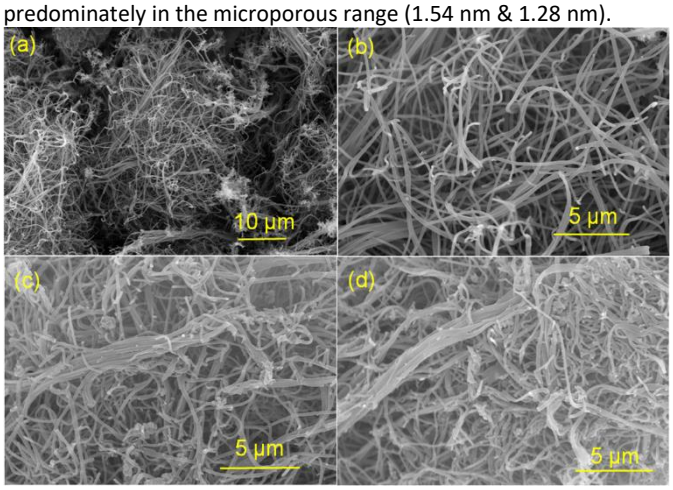

Figure 4: FE-SEM images of (a, b) PPN and (c, d) Pd@PPN materials.

The morphology of the as-synthesized PPN and Pd@PPN materials was investigated by FE-SEM analysis technique (Figure 4). The FE-SEM images of the PPN material mainly consists of homogeneously distribution of self-assembled irregular-shaped

nanofiber-like morphology (Fig. 4a) with the average length of each nanofiber found in the range of 233-333 nm. Similar to PPN material, the Pd@PPN exhibits long-range nanofiber-like morphology with longer folding fibers (length in the range of 406-436 nm) (Fig. 4c)**.** Energy dispersive X-ray (EDX) analysis from the representative FE-SEM image (Figure S4, SI) of the particular selected area consists of spectra (marked with yellow box), signifying relative abundance of each detected element in the specific area. The elemental composition of each element (C, N & Pd) in weight (%) and atomic (%) of Pd@PPN was provided in Fig. S4, SI.

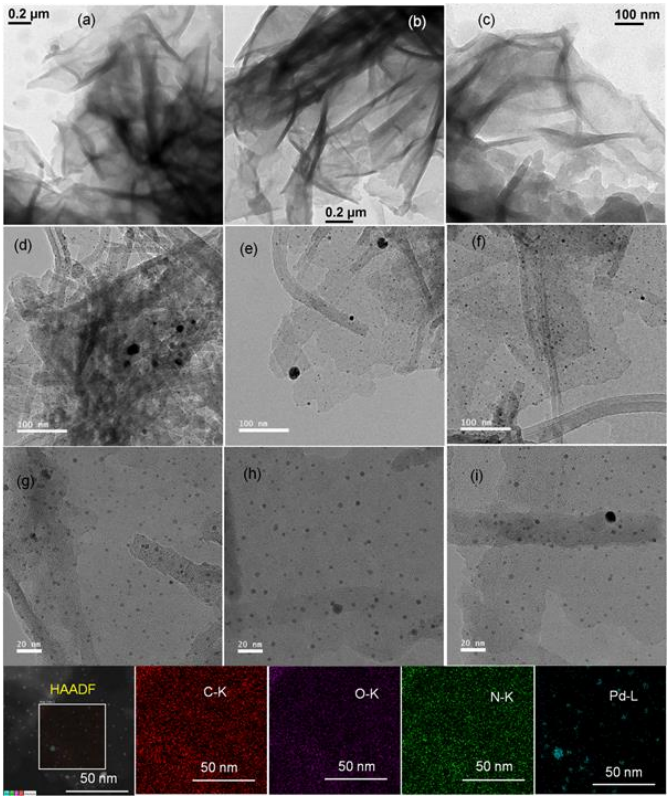

Figure 5: TEM images of PPN (a-c) & Pd@PPN (d-f) at low magnification, (g-i) at high magnification, respectively. HAADF-STEM image of the Pd@PPN with the elemental mapping is also provided.

To examine the distribution, shape, location with mean particle size of Pd NPs on the POP polymer matrix, transmission electron microscopy (TEM) analysis of the PPN and Pd@PPN has been performed and the data are shown in Figure 5. TEM images of the PPN material clearly shows that it consists of thin nanosheets-like morphology having diameter of 33 - 53 nm and length of 207 - 247 nm (Figs. 5a-c) as composed by randomly self-assembled multiple irregular-shaped nanotubes. TEM images of Pd@PPN (Figs. 5d-f) show homogenous spherical Pd NPs with average diameter of 3.2±0.5 nm (Fig. 5f). It is visible from TEM image (Fig. 5d) that PPN fibers of 23-nm-diameter and 284-nm-length are self-assembled to produce a 3D cage like structure in which the small Pd-NPs are strongly anchored. A dual Pd-NPs size distribution with the mean diameter of about 1.86 ± 0.36 and 2.89 ± 0.25 nm is found (Fig. 5g). It is assumed that small size Pd-NPs (1.86 nm) can easily occupy the interior cavities and large Pd-NPs (2.89 nm) are distributed on the external surface of PPN support owing to the inhibition of enormous growth of Pd-NPs by nucleation in the porous channel under solid phase reduction method. This is in good agreement with the previous finding report by Wang and co-workers.[77] Brighter sphere-like spots of diameter 3.4 ± 0.4 nm (HAADF-STEM image, Figure S5, SI) indicate the existence of the metal phases, which are homogenously decorated on the PPN support. Moreover, elemental mapping analysis (Fig. 5) in a selected area of Pd@PPN (marked by white square box), demonstrates that the C (red), O (violet), N (green) and Pd (blue) are nearly distributed at the same location of the PPN phase boundaries.

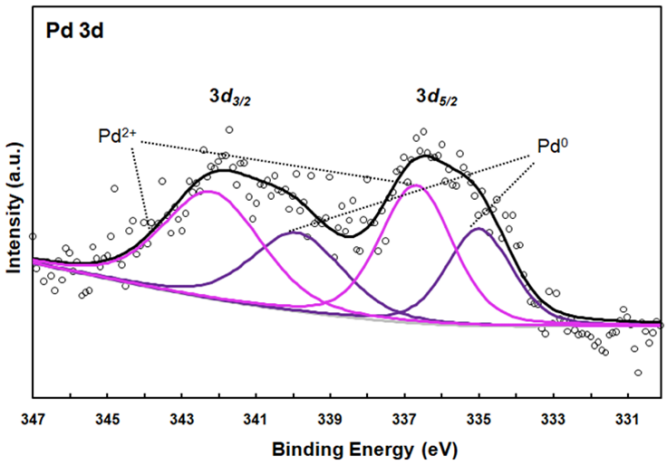

Figure 6: Deconvoluted X-ray photoelectron spectra for the Pd-3d binding energies of Pd@PPN.

In order to evaluate the oxidation state of Pd, XPS analysis of Pd 3d binding energies of the Pd@PPN material was carried out. The appearance of characteristic binding energy peaks of in Pd-3d XPS spectrum (Figure 6) further supports the incorporation of palladium nanoparticles onto the porous surface of PPN polymer material. The high resolution Pd 3d spectrum could be deconvoluted into two sets of spin–orbit doublets corresponding to Pd $3d_{5/2}$ and Pd $3d_{3/2}$ core-level binding energies. The binding energy peaks at 334.68 and 339.58 eV are attributed to the Pd (0) states, which confirms the existing of metallic Pd phase dispersed on the external surface of the PPN polymer material after the treatment in a stream of H_2/N_2. Additionally, the shake-up binding energy peaks at 336.37 and 341.86 eV are attributable to the existence of Pd (II) species in the Pd@PPN polymer material, indicative of the PdO species formation due to the surface oxidation of nano-palladium, a very common phenomenon in noble metals. Besides, XPS analysis also reveals a strong interaction between the well-dispersed isolated Pd species with the frame-structure of PPN through the electron transfer between nitrogen atoms in the PPN and Pd NPs, as was also reported in earlier study.[66] Indeed, a positive binding energy shift by +1.2 eV in the high resolution fitted N 1s XPS spectra (Figure S6, SI) for Pd@PPN in comparison with the as-synthesized PPN has been observed, and it was attributed to the charge transfer of electrons from N atoms to Pd.[81] It also agrees very well with the electronic properties analysis from DFT calculations later.

Catalytic conversion of Vegetable Oils over Pd@PPN Catalyst.

Triglycerides and saturated/unsaturated fatty acids are industrially used in bio diesel and soap preparation. We selected stearic acid as the model compound in order to check the catalytic activity of Pd@PPN catalyst to generate diesel additives. Liquid phase hydrogenation of stearic acid gives rise to the *n*-heptadecane (C17 alkane), *n*-octadecane (C18 alkane), *n*-octadecanol (C18-OH) and a very small amount of other cracking products. From literature, the process of alkane formation may involve three different routes.[19, 30, 70, 82, 83] The first pathway is the initial hydrogenation of fatty acid to alcohol along with the subsequent hydro-dehydration and produces the corresponding alkane with the same number of carbon as the initial fatty acid. The other two remaining routes involves the direct decarboxylation pathway (CO_2 removal) of fatty acid and the decarbonylation pathway (CO removal), both produce the alkane with one carbon less in the hydrocarbon chain. Previous studies reported that the hydrogenation-hydrodehydration pathway is more feasible at low temperature and low pressure, while the decarbonylation/decarboxylation pathways are more feasible at high temperature and high pressure.[30]

Firstly, we investigate the distribution of reactant and products of the catalytic hydrogenation of stearic acid over Pd@PPN catalyst as a function of time and the results are presented in Figure 7a. In this investigation, the hydrogenation reaction of stearic acid (100 mg, 0.350 mmol) was carried out in water (70 mL) over Pd@PPN catalyst in a stainless-steel reactor under 20 bar hydrogen pressure, at 150 °C temperature for 16 h (the choice of reaction parameters such as temperature and pressure are also investigated and optimized in Figs. 7b,c). The reaction was monitored by GC-FID technique based on actual authentic sample. At the initial 1 h of reaction, only 7% conversion of stearic acid with significant amount of stearyl alcohol (45%), a moderate amount of C18-alkane (15% selectivity) and very negligible quantity of C17-alkane and other cracking products with 5% and 2% selectivity were achieved. At 4 h of reaction, the conversion of stearic acid was 30% and the selectivity of stearyl alcohol reaches its maximum of 78%, while the selectivity of C18-alkane and C17-alkane were 9% and 19%, respectively, indicating the formation of stearyl alcohol as a primary product via hydrogenation at the first step of the reaction. With the advancement of the reaction, the selectivity of the stearyl alcohol significantly dropped to 7% with the increase of C17 selectivity (78%) along with negligible amount of C18 (9%) furnished after 6 h course of the reaction. After 10 h of reaction, C17 alkane is the major product with high selectivity (81%), while small amount of C18 alkane (10% selectivity) and insignificant amount of stearyl alcohol (1% selectivity) were observed. The diminishment of the stearyl alcohol selectivity was observed after 12 h with 89% of stearic acid conversion and 82% C17 alkane selectivity. We also noticed that 90% of stearic acid conversion along with 83% C17 selectivity was observed with the prolongation of reaction time up to 14h, and is not much improved after that. Therefore, the optimized reaction time was chosen of 14 h for screening the effect of other reaction parameters (temperature and H_2 pressure) later. Besides, it could be observed that the formation of C17 alkane is more favorable than C18 alkane on our fabricated Pd@PPN catalyst, demonstrating the preference of decarboxylation/decarbonylation pathways over the hydrogenation-hydrodehydration mechanism and therefore only the decarboxylation/decarbonylation mechanisms will be evaluated by DFT simulations in later sections.

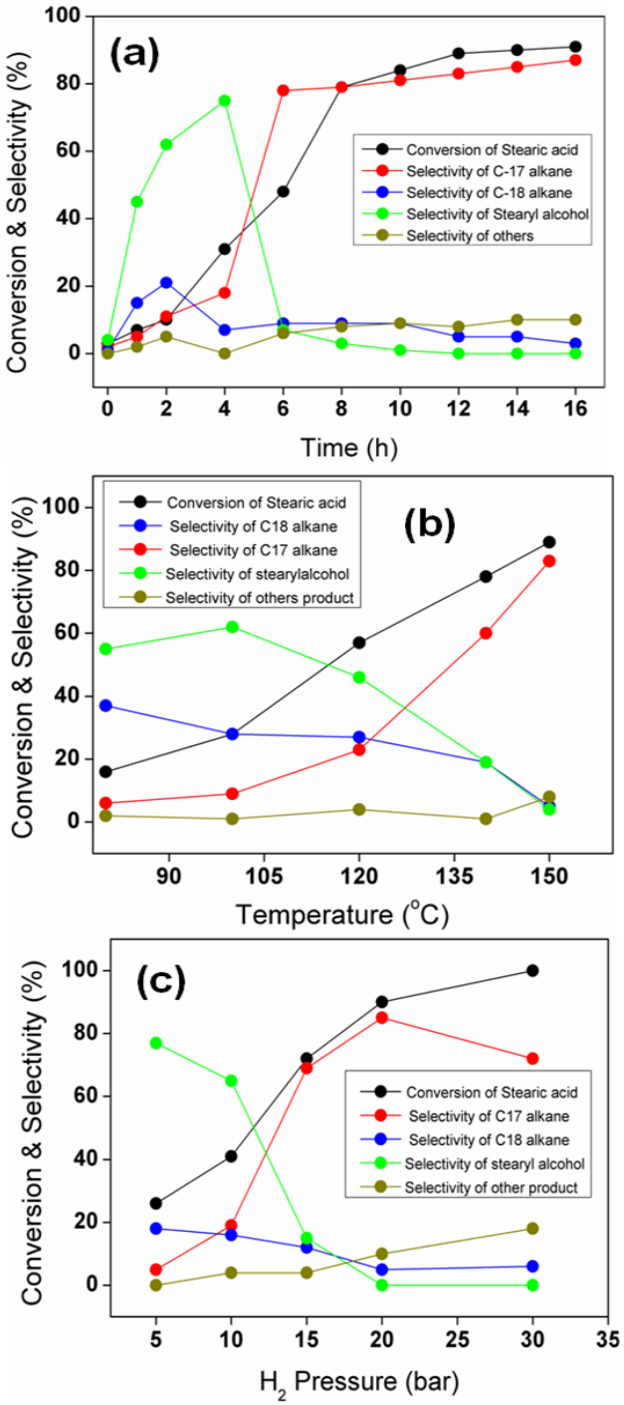

Figure 7: Evolutions of reactant and product distributions for stearic acid hydrogenation over Pd@PPN catalyst as a function of time (a); temperature (b) and H_2 pressure (c). Reaction conditions: stearic acid (100 mg, 0.350 mmol), Pd@PPN (20 mg, 2.6 mol % of Pd feed), water (70 mL). The designation "other products" denotes the cracking products, smaller alcohols and esters.

To investigate the effect of reaction temperature on the selectivity of stearyl alcohol, C17 and C18 alkanes, a series of reaction were carried out under different temperatures (ranging from 80 to 150 °C) as shown in the Fig. 7b. It could be seen that both the conversion of stearic acid and the selectivity of C17-alkane are increased with increasing temperature. This observation suggests that high reaction temperature favours the formation of C17 alkane via the decarbonylation/decarboxylation pathway. Srifa *et al.* reported that C17 alkane was formed from the intermediate stearyl alcohol by the decarbonylation/decarboxylation reaction, which are supposed to be equilibrium with stearyl alcohol during the HDO process.[84] In constrast, increasing temperature decreases the selectivity of the stearyl alcohol gradually from 55 % (at 80 °C) to 4 % (at 150 °C). It is supposed that the production of C18 alkane via stearic acid hydrogenation by the alcohol pathway is an endothermic reaction, while the decarbonylation/decarboxylation to C17 alkane is an exothermic reaction.[30] The high temperature is generally preferred to execute the first, while low temperature is convenient for the second pathway.[29] Almost complete conversion of stearic acid (90%) with 83% selectivity on C17 alkane, about 5% of C18 alkane and insignificant amount of stearyl alcohol (C18-OH) and cracking products were generated at 150 °C.

Finally, the influence of H_2 pressure (from 5 bar to 30 bar) on the catalytic conversion of stearic acid was also studied and the result is presented in the Fig. 7c. It is important to note that when the reaction was conducted under Ar atmosphere (no H_2 pressure), we observed only 0.2 % of C17 product. When the reaction was conducted under the H_2 pressure of 5 bar, only 26% conversion of stearic acid and 77 % selectivity of stearyl alcohol (C18-OH), 18% of C18 alkane and 5% of C17 alkane were obtained. However, the product distribution is significantly changed at higher pressure (Fig. 7c). When the reaction was carried out under 15 bar H_2 pressure, 72% conversion of stearic acid was achieved with 69% selectivity of C17 alkane while the selectivity of stearyl alcohol (C18-OH) and C18 alkane were significantly reduced to 15% and 12%, respectively. An abrupt increment in C17 alkane selectivity observed after 15 bar pressure suggests that decarboxylation/decarbonylation pathways are encouraged at high H_2 pressure, in good agreement with the previous literature reports.[85] At the optimized H_2 pressure of 20 bar, 90 % conversion of stearic acid along with selectivity of 83% for C17 alkane, 5% for C18 alkane and 10 % for other product was acquired. When the H_2 pressure was increased to 30 bar, the complete conversion of stearic acid was observed, however the selectivity of C17 alkane was reduced to 72% along with the increment of cracking products with 18% selectivity, indicating the degrading of decarbonylated product at higher pressure via cracking reactions, which was also reported in earlier study.[31] H_2 pressure also takes part in improving the catalyst against deactivation, as it prevent the oligomerization of unsaturated hydrocarbons by hydrogenation them to the corresponding alkanes, thus hinder the formation of coke in the reaction medium.[86]

To understand the role of PPN to the activity of Pd-NPs, a series of Pd-NPs based catalytic model hosted on the various supports including SiO_2, C, TiO_2, and ZrO_2 were investigated under the same above-mentioned optimized reaction conditions. The evolution of reactant and product distributions with the selectivity of C17 alkane, C18 alkane, C18 alcohol (stearyl alcohol), other cracking products (≤ C16 alkanes), and ester is tabulated in the Table 1. It is noteworthy that all the catalysts were prepared following a similar catalyst synthesis procedure. Data in Table 1 demonstrated that Pd@PPN catalyst exhibited the best performance among all the examined Pd catalysts. Pd@SiO_2, Pd@C, Pd@TiO_2, and Pd@ZrO_2 catalysts furnished the desired C17 alkane product with the selectivity of 8.7%, 41.3%, 10.5% and 33.8%, respectively. The poor selectivity of C17 alkane in comparison with C18 alkane for Pd@SiO_2 catalysts revealed that hydrodehydration reaction pathway is promoted with the surface acidity of the SiO_2 support. Similar finding on the surface acidity promotion of hydrodehydration route with Ru@TpPON catalyst was reported by Bhaumik and co-workers.[29] In strong contrast, we achieved higher C17 alkane selectivity for Pd@PPN in comparison with the Pd@C catalyst (Entry 2, Table 1). This result could be attributed to the electron rich Pd-NPs, which may activate surface bound H_2 on the high catalytic performance.[87] Pd@ZrO_2 possessed poor activity and gave alcoholic products (entry 4, Table 1), possibly due to the poor dispersion of nanoparticles, weaker metal-support interaction, low surface area, and low mass transfer. Furthermore, in order to investigate the structural sensitivity of the Pd@PPN catalyst for the HDO of carboxylic acids, we have synthesized another catalyst using the liquid phase reduction method (details of this catalyst synthesis are provided in the SI). By this way, we were managed to synthesize another Pd NP hosted in the Porous-Organic-Polymer (called Pd@PPN-1) where the size of Pd-NPs was ~8.9 nm as evidenced from the TEM images analysis (Fig. S7, SI). For this catalyst, we achieved only 63.7% conversion of stearic acid towards 51.3% selectivity of C-17 (Entry 6, Table 1), much lower than the smaller Pd@PPN catalyst with the particle size of 3 nm. The observed results show that the HDO conversion of carboxylic acids on Pd@PPN catalysts is structural sensitive, and is also consistent with the high activity of step sites presented in large density on the smaller size Pd@PPN, which will be discussed later.

Table 1: Comparison of stearic acid conversions over different Palladium-based catalysts

Entry	Catalyst	Conversion (%)	Selectivity (%)			
			C17 alkane	C18 alkane	C18 alcohol	Others
1	Pd@SiO_2	56.8	8.7	29.5	9.5	9.1
2	Pd@C	63.2	41.3	9.3	5.1	7.3
3	Pd@TiO_2	49.7	10.5	37.6	1.5	0
4	Pd@ZrO_2	64.5	5.1	10.6	48.7	0
5	**Pd@PPN**	**89.6**	**83.5**	**6.1**	**0**	**0**
6*	**Pd@PPN-1**	**63.7**	**51.3**	**12.4**	**0**	**0**

Reaction conditions: Stearic acid (100 mg, 0.350 mmol), Pd-catalyst (20 mg, 2.6 mol% of Pd feed), water (70 mL), 150°C, H_2 (20 bar), 14 h. *The size of Pd-NPs in Pd@PPN-1 is ~8.9 nm.

As different vegetable oils comprise unique compositions of fatty acids and impurities, we selected four typical commercialized oils, *i.e.* palm oil, soybean oil, sunflower oil, and rapeseed oil. These oils are subjected for hydrogenation treatment with Pd@PPN catalyst under optimized reaction

conditions (Figure 8). The fatty acid compositions of these oils are listed in the respective Table T2, SI. Corresponding alcohols and esters intermediates of the present saturated fatty acids were identified at the initial reaction course, followed by progressive increase yield of respective alkanes with the further advancement of catalytic reaction. Mechanistically, unsaturated fatty acids (oleic acid, linoleic acid) consisting of the double bond can be easily transformed into their corresponding saturated analogue under the present reaction conditions. Acyl C-O bond cleavage is likely to occur resulting in alcohol intermediate followed by hydrogenolysis. Another competitive decarbonylation/decarboxylation route of the aldehyde intermediates leading to the formation of alkanes with one carbon atom less is also associated.[14]

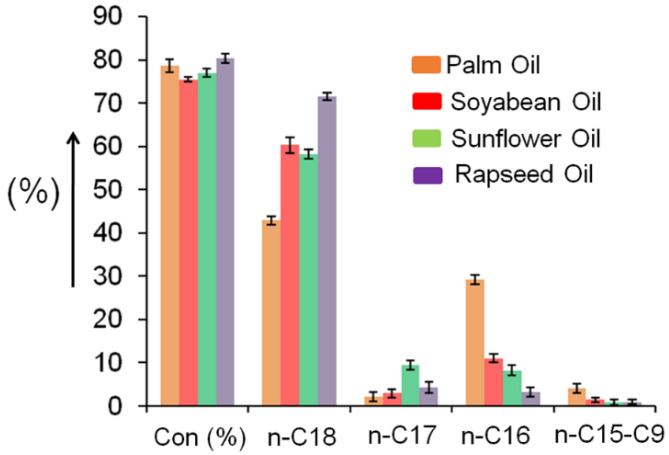

Figure 8: Hydrogenation of various vegetable oils over Pd@PPN catalyst. Reaction conditions: Vegetable Oils (0.2 g), Water (70 mL), 150 °C, 20 bar H_2 pressure, Time 14 h, Catalyst (100 mg, 13.07 mol % of Pd feed).

Stability testing.

We performed recyclability study of the newly designed Pd@PPN catalyst to evaluate stability under optimized reaction conditions considering stearic acid as model compound (Figure S8, SI). After each use, the black powder Pd@PPN was isolated by centrifugation followed by washing with methanol (three times) and acetone (two times), drying at 100 °C in an oven for 8 h. A significant drop in stearic acid conversion from 90.5% to 76.8% was observed after five runs. Besides, a significant decrease of the C17 alkane selectivity from 85.8% to 69.4% occurred along with the gradual enhancement in the stearyl alcohol (C18-OH) selectivity from 10% to 25% (Fig. S8, SI). A drop in the efficiency of Pd@PPN catalyst could be attributed to the accumulation of carbonaceous deposits on the catalyst surface or slight trapping of residual reactants or products inside the pores, thus blocking accessibility to the active sites. The location, distribution, and size of the Pd-NPs of the reused catalytic systems have been investigated by conducting TEM analysis at 4th and 5th catalytic cycles, respectively in Figure 9.

Dual size distribution of Pd NPs over carbonaceous PPN nanotube was observed after 4th catalytic run with the uniform distribution in the range of 3.2 - 4.0 nm and 7.4 - 11.4 nm, respectively (Fig. 9a-c). Surprisingly, after 5th catalytic run Pd-NPs size increases enormously to 15 - 19.5 nm and 24 - 31 nm (Fig. 9d-f), which could be attributed to the diffusion of particles out of the interior cavities and their deposition over external facet. Increasing of average particle size and its severe aggregation after 5th cycle (Fig. 9d) caused the drastic drop in stearic acid conversion from 90.5% to 76.8%. The surface and morphology of the PPN nanotube was unchanged after the 4th and 5th catalytic cycle although the width of the nanotube was a little bit enlarged after each cycle compare to the fresh one. The PPN structure proved to be stable with no associated structural degradation. To examine any leaching that took place during the reaction, we conducted a hot-filtration test under optimized reaction conditions. ICP-AES analysis results suggest the Pd content in the reused Pd@PPN catalyst after the fourth and fifth catalytic runs are 0.413 and 0.397 mmol/g, respectively, which validated that that there was an insignificant leaching of Pd species. In addition, the ICP-AES results of both the used catalyst and the solution after reaction (with consideration of experimental error) definitely revealed that the Pd-NPs were barely leached in this reaction system owing to strong attachment with highly cross-linked interconnected a three-dimensional rigid framework at the molecular level.

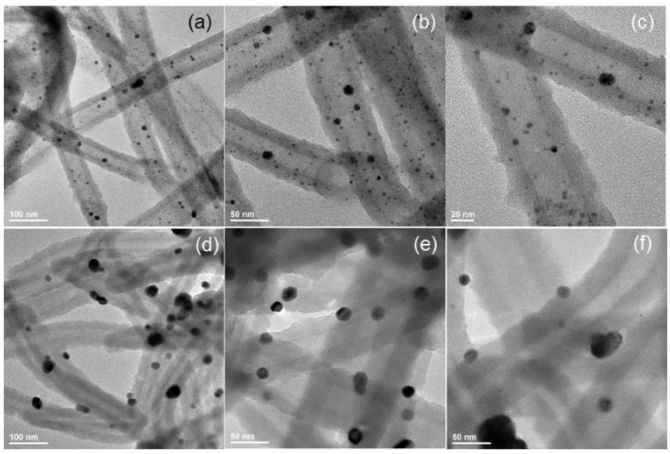

Figure 9: TEM images of used Pd@PPN catalyst after 4th (a-c) and 5th (d-f) catalytic runs.

Formation of high density step sites on Pd@PPN

To gain more information on the interaction between Pd NPs and the polymer structure, we studied the interaction of the monomer unit of the polymer, called *um*PPN molecule, onto the surface of Pd NPs using the reduced-cluster model of 3 nm particle size (Fig. 2c). Note that this size of 3 nm was also characterized using TEM image as shown in Fig. 5d. As mentioned earlier in the literature, the interaction between benzene ring and Pd(111) surface was determined as the combination between covalent bond and long-range vdW interaction, making the very strong binding of aromatic rings on flat Pd surface.[54] Six different adsorption configurations of *um*PPN with the Pd_{332} cluster are presented in Figure 10 and the binding energies relative to the adsorption energy of the most stable configuration are indicated. In the most stable configuration in Fig.10a, *um*PPN binds to the Pd_{332} cluster via the interaction of 5 aromatics rings (2 rings from each TPA fragment and 1 ring from the p-xylene fragment). In this configuration, two TPA fragments of *um*PPN both are adsorbed at two corner sites of the Pd_{332} cluster. If *um*PPN binds to the Pd_{332} cluster via the interaction of only 4

aromatics rings in Fig. 10b (2 rings from the first TPA fragment at the corner, 1 ring from the p-xylene fragment and only 1 ring from the other TPA fragment), the binding energy is +56 kJ/mol less stable than configuration (a). In case *um*PPN still binds to the Pd_{332} cluster via the interaction of 4 aromatics rings but the first TPA adsorbs at steps site instead of corner site (Fig. 9c), the binding energy is +71 kJ/mol less stable than configuration (a). If the benzene rings from p-xylene and from the second TPA fragment do not participate into the interaction, the binding energies become significantly weaker by +299 kJ/mol and +323 kJ/mol, where *um*PPN binds to the Pd_{332} cluster via the interaction of only 2 aromatics rings (Figs. 9e,f). Finally, the least stable configuration is when *um*PPN molecule adsorbs on flat terrace sites via the coordination of only one aromatic ring of one TPA fragment (Fig. 9d), and the computed binding energy for this configuration is +359 kJ/mol weaker than in Fig.9a. It could be observed that the more benzene rings of *um*PPN interacting with the Pd_{332} cluster, the more stable is the interaction. In the most stable configuration in Fig. 9a, the computed binding energy is ~-587 kJ/mol. From the top-view of configuration in Fig. 9a, one full unit monomer *um*PPN of the polymer structure nicely covers and wraps around one exposed facet of the Pd_{332} cluster, which could explain consistently the size of 3nm for Pd NPs anchoring on the polymer substrate. Besides, the strong interaction of Pd cluster with the frame structure of the polymer at the step-edge and corner binding modes could be a factor generating high density of step sites for the fabricated Pd NPs. Due to the non-planar structure of TPA fragments (three benzene rings are tilted forming corrugated structures) and the very strong binding of aromatic rings to Pd terrace facets, the as-synthesized Pd NPs could be nucleated at corrugated sites formed by TPA fragments, and then grew along the chain of benzene rings and finally formed the NPs structure with lots of surface corrugations and high density of step sites. It is important to note that although the monomer unit prefers adsorption at the corner and step edges, the steric effect could prevent the monomers adsorb in close vicinity to each other. Therefore, the coverage of the monomer at step edge might not be high enough to block all step sites, and there is still a large portion of free step sites on the Pd NPs (details explanation is presented in Fig. S16, SI). The presence of step sites with high density consequently could be one of the important factors contributing to the high activity of the Pd@PPN for the HDO conversion of fatty acids. The next sections will therefore evaluate the activity of those step sites in the HDO reactions.

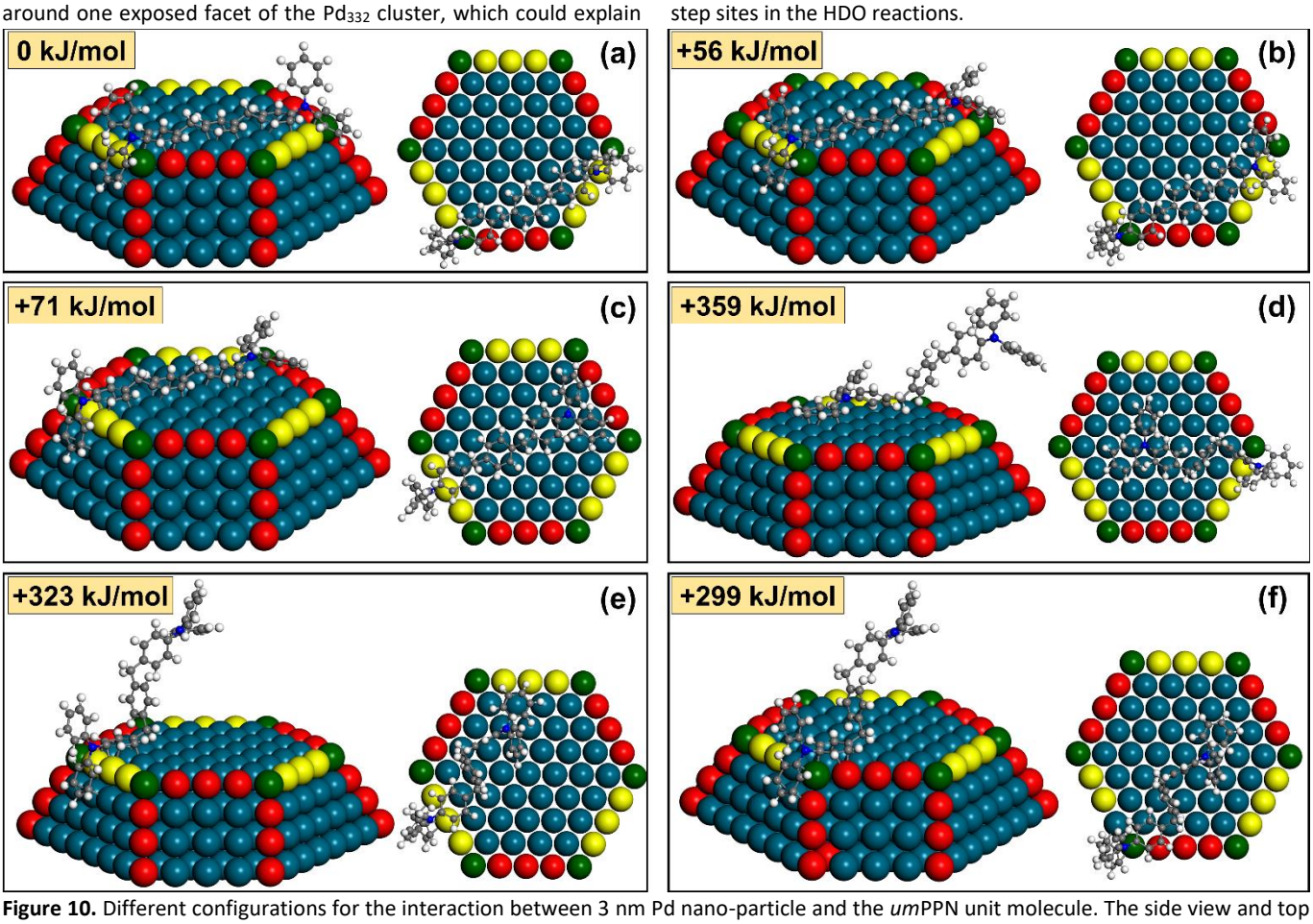

Figure 10. Different configurations for the interaction between 3 nm Pd nano-particle and the *um*PPN unit molecule. The side view and top view are presented for each configurations. Binding energies relative to the most stable configuration (configuration a) are also shown. F4, B5 step sites and corner site are highlighted by big yellow, red and green balls, respectively.

Mechanistic study on the conversion of butanoic acid on Pd@PPN.

HDO conversion of butanoic acid on terrace sites of Pd(111). The mechanism for HDO reaction of linear chain acid on Pd(111) surface has been comprehensively studied in literature.[70, 82, 83] It is widely accepted that there are three possible mechanisms for the HDO of carboxylic acids: (i) the decarbonylation (DCN) pathway where oxygen atoms are removed from the initial carboxylic acids reactant in the form of CO, (ii) the decarboxylation (DCX) where oxygen atoms

are removed in the form of CO_2 and (iii) the reductive deoxygenation (RDO) where oxygen atoms are removed in the form of water (also called as hydrogenation-hydrodehydration pathway). In the first two cases, the number of carbon atoms in the products is one atom less than in the reactant molecule while for the last case, the number of carbon atoms of the product remained identical as the initial reactant. There is a general agreement from experimental studies in literature that Pd-based catalyst favors the DCX and DCN pathway of carboxylic acids over the RDO pathway in producing the product with one less carbon atom.[88-91] Besides, to facilitate the RDO mechanism, more hydrogen is consumed, however its supply is being in short in refineries and facing growing demand for other competitive applications such as CO_2 reduction, fuel cell… and therefore developing the catalyst that can facilitate the RDO pathway is less desirable.[92-94]

There is a known competition between the DCX and DCN pathways on Pd(111) surface. Using propanoic acid as the model compound and performed DFT simulations on Pd(111) surface, Lu *et al.* reported that the DCX and DCN pathways were initiated by the OH activation and Cα-H activation, respectively.[70] By evaluating the detailed microkinetic modelling, the authors reported that the DCN mechanism is more feasible than the DCX one. The initial C_α-H activation and the subsequent dehydroxylation scission of the CO-OH bond were identified as the rate-determining steps during the DCN pathway.[70, 82] Actually, the crucial role of C_α-H activation as the precursor to facilitate the DCN pathway was also confirmed in the kinetics isotope study of deuterium-labelled propanoic acid HDO over Pd catalyst by Lugo-Jose *et al.*[83] Besides, the removal of strong-bound intermediates or products such as unsaturated hydrocarbons (via hydrogenation) and CO was also stated as one of the "bottle-necks" hindering the rate of conversion.[82]

To setup the reference for evaluating the activity of steps sites during the HDO on Pd@PPN catalyst, we revisited the activation and conversion of fatty acid on Pd terrace sites of the p(4×4) Pd(111) periodic slab model via both DCX and DCN pathways using butanoic acid as the model compound. It is important to note that in this study we followed the most possible mechanism for the DCX and DCN pathways that were identified and reported for HDO of propionic acid on Pd(111) surface in Luo et al.[70, 82] The scheme of reactions, together with the transition states and activation barriers for the reactions along those pathways are presented in Figure 11. Note that the reactions along this scheme are the most feasible occurring at each steps, and other less kinetically feasible reactions are shown in SI. Butanoic acid adsorbs on Pd(111) surface with an adsorption energy of -83 kJ/mol (Figure S17a). Three possible initial activations of butanoic acid in Fig. 11 could open three different pathways of the HDO. If butanoic acid is processed via the initial C_α-H activation with the barrier of 117 kJ/mol (TS1-1, Fig. 11), then the HDO conversion follows the DCN pathway. Subsequent reactions along the DCN pathway are the C_β-H activation at the 2nd step with a barrier of 81 kJ/mol (TS2-1), followed by the subsequent dehydroxylation in step 3 with activation barrier of 112 kJ/mol (TS3-1). The DCN reaction is then occurred in the next step 4 with computed activation barrier of 91 kJ/mol (TS4-1, Fig. 11), releasing CO and forming the C_3 hydrocarbon product. However, the most feasible initial activation of butanoic acid on Pd(111) surface is the OH activation with a barrier of 63 kJ/mol (TS1-2, Fig. 11), which initiated the DCX pathway. Subsequent conversion of butanoic acid processed along the DCX mechanism includes the C_α-H activation at the 2nd step after initial OH dissociation (barrier energy of 131 kJ/mol, TS2-1) and the decarboxylation reaction step 3 with the barrier of 99 kJ/mol (TS3-1, Fig. 11), releasing CO_2 and forming the C_3 hydrocarbon product. As could be seen, the C_α-H activations (TS1-1 and TS2-2) play an important role in both DCX and DCN pathways, agrees very well with the data reported earlier and is also consistent with experimental observations in the literature.[10, 82, 83] It is important to note that regardless of the more favourable pathway, both the DCX and DCN pathways produce the same alkane product with one less carbon than from the carboxylic acid feedstock. Furthermore, if the HDO is processed via the DCN pathway, the Water Gas Shift reaction could also convert the produced CO to CO_2, the same products of the DCX pathway, therefore it is very challenging to distinguish between DCX and DCN pathway by experiments.

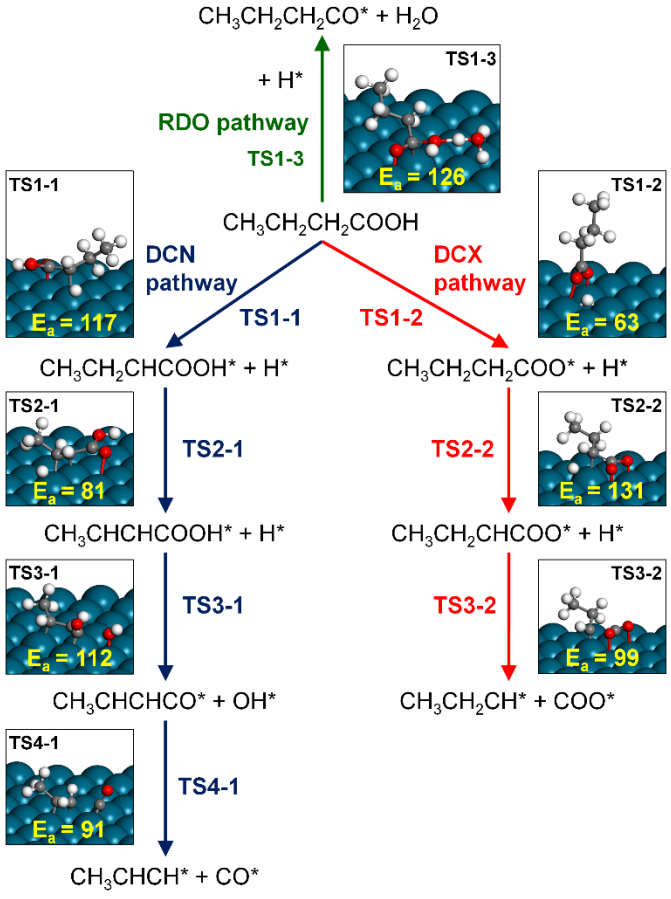

Figure 11. Hydrodeoxygenation (HDO) of butanoic acid on Pd(111) surface via three different pathways. Reactions along the Decarbonylation (DCN) pathway are indicated by blue arrows, while reactions along the Decarboxylation (DCX) pathway are indicated by red arrows. The reductive deoxygenation (RDO) pathway is indicated by green arrow.

The third pathway for the HDO of butanoic acid is the reductive deoxygenation (RDO) pathway, which produce the final alkane product with the same carbon atom as in carboxylic acid resource. This pathway is initially processed by the hydrogen-shuttling mechanism, where water acts as a hydrogen shuttle to transfer the adsorbed H on Pd(111) surface to the OH group of butanoic acid and facilitating the dehydration, forming H_2O. The activation barrier for this reaction is 126 kJ/mol (TS1-3, Fig.11). However, it should be mentioned that this type of H-shuttling reaction will suffer from extra entropic energy penalty for locating the water molecule to the exact positon in the transition state, as was reported by Gunasorria *et al.*[95], making it less favourable compare to the DCX and DCN pathways and will only be feasible at high enough pressure of hydrogen. This observation could explain the high selectivity towards the DCX and DCN pathways obtained from the HDO of carboxylic acids obtained in our study. There are other reactions could occur during the initial step of RDO pathways, but with higher barriers and therefore less competitive and are described in Figures S18 and S19 of the SI.

HDO conversion of butanoic acid on Pd step sites. The model of p(4x8) with 4 missing rows on the top layer is used to evaluate the activity of Pd step sites. It is worth to mention that in this model, there are the presence of extended terrace sites next to the B5 and F4 step sites and is an excellent representative for the 3 nm particle model. This model has more active sites and is therefore more appropriate than the use of periodic Pd(211) surface in literature. We have evaluated the activities of B5 steps site and F4 steps site for few reactions of butanoic acid and found that their activities are quite similar (Figure S20, SI). Therefore, we only present the data observed at B5 step sites to discuss the activity of step sites in HDO reaction. The HDO energy profiles for butanoic acid conversion on Pd terrace site and step site are presented in Figure 13, while the structure of the transition states along those pathways are shown in Figure 12.

Firstly, we investigated the initial activation of butanoic acid. Butanoic acid adsorbs at B5 step site with an adsorption energy of -95 kJ/mol (Fig. S20a, SI), which is 22 kJ/mol stronger than it is on flat terrace site. Initial OH activation at B5 step site is slightly promoted with the barrier of 56 kJ/mol (TS1-2, Fig. 12b), compared to 63 kJ/mol at flat terrace site (Fig. 11). However, the initial C_α-H activation is much stronger promoted at step site, and the barrier of this activation is brought down from 117 kJ/mol at terrace site to only 79 kJ/mol at step site (TS1-1, Fig. 12a). Interestingly, the hydrogen-shuttling reaction that initiates the RDO pathway in Fig. 11 is not structural-sensitive, and the activation barrier for this reaction on Pd B5 step site is 121 kJ/mol (TS1-3, Fig. 12c). Another competitive two-step Hydrogenation-dehydroxylation mechanism for the RDO pathway, which is not feasible on terrace site (Figure S19, SI) but strongly promoted on step site, is discussed in Figure S23, SI. Nevertheless, the barrier of that reaction is still higher than the hydrogen-shuttling mechanism. From all possible activations in the initial step, the OH activation is still the lowest barrier reaction, however, the C_α-H activation now has the barrier energy much closer to the OH activation. The difference between barrier energy for the initial OH activation and C_α-H activation for reaction occurred at step sites is only 23 kJ/mol compared to a much bigger gap of 54 kJ/mol on normal terrace site of Pd(111) surface. Therefore, Pd step sites promote the initial C_α-H activation much stronger than the initial OH activation and will have great impact to facilitate the preference of DCN pathway over the DCX pathway.

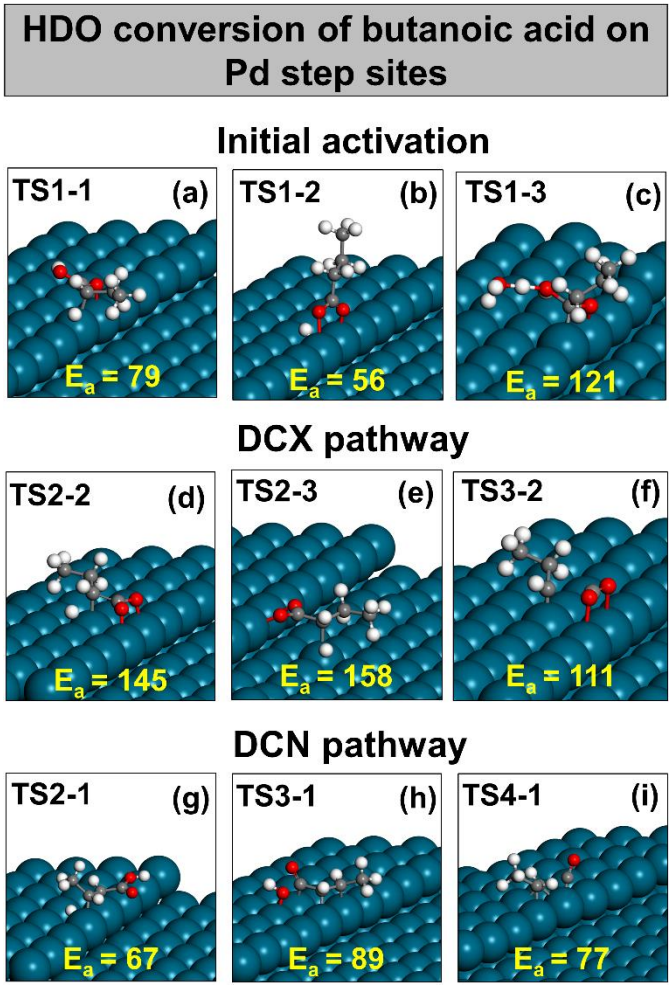

Figure 12. Activation and HDO conversion of butanoic acid via DCX and DCN pathways at Pd B5 step sites. (a) Initial Cα-H activation; (b) Initial O-H activation; (c) Initial hydrogenation-dehydration reaction. The subsequent conversion of butanoic acid along the DCX pathway after the initial O-H activation: (d) C_α-H activation on upper terrace sites in step 2; (e) C_α-H activation on lower terrace sites in step 2; (f) Subsequent decarboxylation reaction (-CO_2) in step 3. The conversion of butanoic acid along the DCN pathway at Pd B5 step sites after initial Cα-H activation: (g) subsequent C_β-H activation in step 2; (h) CO-OH scission in step 3; (i) decarbonylation (-CO) reaction in the 4th step.

Next, we evaluate the subsequent reactions along the DCX pathway for the butanoic acid HDO at step site, which is processed via the initial OH activation, follow the similar mechanism occurred on normal terrace sites of Pd(111) surface as showed in Fig. 11. Surprisingly, almost subsequent activations in step 2 of the DCX pathway at step sites become more difficult than they are on normal terrace sites of Pd(111) surface. The product of initial OH activation, butyrate, adsorbs on step site in the bidentate configuration and

coordinate to the step site via both two O atoms as shown in Fig. S21b. Due to the stronger binding of butyrate on step sites (39 kJ/mol stronger than its binding energy on terrace site), a noticeable energy penalty is needed to bend the adsorbed molecule closer to the surface for further activations of C-H bonds or C-C scission, resulting in higher activation barriers for almost all reactions in step 2 of the DCX pathway. As shown in Figs. 12d,e, C_α-H activation has the higher barrier of 145 kJ/mol if processed by upper-terrace sites next to B5 site (TS2-2, Fig. 12d), or 158 kJ/mol if processed by lower-terrace sites next to B5 site (Fig. 12e). Other reactions in step 2 are also have higher barriers than they are on terrace site (Fig. S21c,d, SI). The same trend is also found in the decarboxylation reaction releasing CO_2 in step 3 (barrier of 111 kJ/mol, TS3-2, Fig. 12f), which is 12 kJ/mol higher than the reaction on normal terrace site of Pd(111). The high barriers of reactions in step 2 and the increment in activation barrier for the subsequent decarboxylation reaction make the reactions along the DCX mechanism more sluggish and therefore, the DCX pathway is kinetically more hindered at step sites.

The DCN pathway is initiated by the C_α-H activation of butanoic acid, which is strongly promoted at step site. Similar to the mechanism occurred on normal terrace site of Pd(111) surface, subsequent reactions along the DCN pathway are also kinetically feasible and slightly promoted at step sites. The step 2 consists of the C_β-H activation with activation energy of 67 kJ/mol (TS2-1, Fig. 12g), which is 14 kJ/mol lower than on normal terrace site. After the C_β-H activation in step 2, the product has the conjugated structure CH_3-CH=CH-COOH and the dehydroxylation reaction from this molecule in step 3 can be processed with barrier of 89 kJ/mol (TS3-1, Fig. 12h), forming the ketene-type product CH_3-CH=CH-C=O. The subsequent decarbonylation reaction in step 4 releasing CO and hydrocarbon product with one carbon atom less is also very feasible with activation barrier of only 77 kJ/mol (TS4-1, Fig. 12i).

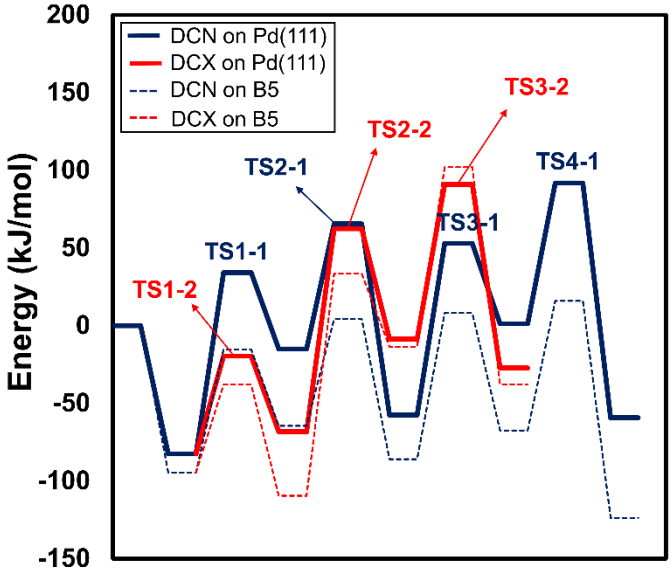

Figure 13. Energy profiles for HDO conversion of butanoic acid on terrace sites (Pd(111)) and on step sites (B5). Reactions along the DCN and DCX pathways are indicated in blue and red colours, respectively. Reactions on terrace sites and step sites are indicated by solid lines and dash lines, respectively.

The energy profiles for the conversion of butanoic acid via DCX and DCN pathways on terrace site and step sites are presented in Figure 13. Overall, it could be seen that Pd step sites strongly promote the rate-limiting step during the DCN pathway (initial C_α-H activation TS1-1 and later dehydroxylation reaction TS4-1) and also in the same time inhibits the competitive DCX pathway. Although both the DCX and DCN pathway could all produce the same alkane product, we could infer from the energy profiles presented in Fig. 13 that the DCN pathway of fatty acids HDO process on the Pd@PPN material might become more dominated than the DCX pathway, however it is still very difficult to be validated by experiment. It is also worth noting that the density of step sites is a function of particle size, and is reduced drastically when particle size is larger than 3 nm (the density of B5 step sites on 8 nm particle is only 15% of the density of B5 step sites on 3 nm particle).[58] For other catalysts in Table 1 that also can facilitate the DCN/DCX pathways to produce alkane with one less carbon atom from the carboxylic acid resource such as Pd@C (entry 2) and Pd@PPN-1 (entry 6), their particle sizes are also in the range of ~9 nm (Figure S7, SI). Therefore, the density of step sites on the fabricated Pd@PPN catalyst (particle size 3 nm) is much larger and resulting in the significant higher conversion of stearic acid and very high selectivity of C-17 hydrocarbon product on our Pd@PPN catalyst compared to other Pd-based catalysts as presented in Table 1. The fact that (i) there is the presence of high density of step sites on Pd@PPN material and (ii) both of those rate-limiting reactions are all promoted at Pd step sites could result in very high activity of Pd@PPN for the HDO reaction.

Electronic properties of Pd@PPN.

To gain more understanding about the charge transfer between Pd NP and the polymer frame structure, the Bader chargers of all atoms in the isolated *um*PPN molecule and for the adsorption of *um*PPN on Pd_{332} cluster are calculated. The charges of several Pd atoms on the Pd_{332} cluster coordinated with adsorbed *um*PPN in its most stable configuration as shown in Fig. 10a, and the changes of the Density of states projected on d-orbital (PDOS) for the corner Pd site interacting with *um*PPN referenced to the clean Pd NP are shown in Figure 14.

In the isolated *um*PPN molecule, the charges of N atoms are -1.24. However, when *um*PPN is adsorbed on the Pd_{332} cluster in its most stable configuration (Fig.10a), the computed charges on N atoms are -1.12, which is more positive (less negative) than the charge of N atom in the lone *um*PPN. Since the XPS chemical shift is very sensitive to the charge transfer[96, 97], the more positive charge induced on N atoms in Pd@*um*PPN than in the lone *um*PPN structure therefore is excellently consistent with the positive shift of N 1s core-level binding energy by +1.2 eV observed in the experimental XPS spectra for Pd@PPN in comparison with the as-synthesized PPN (Fig. S6, SI).

More information about the interaction between Pd-NP and the polymer frame structure could be revealed when we analysed the charge of Pd atoms and their Projected Density of States (PDOS). The charge of the Pd corner site on the clean Pd-NP is -0.043, but is changed significantly to +0.144 after interacting with the *um*PPN molecule, as is shown in Fig. 14a. The withdrawal of electron from the Pd corner site is consistent with PDOS of it on clean Pd-NP and

on Pd@*um*PPN as shown in Fig. 14b, evidenced from the reduce from 92% to 88% for the d-orbital occupancy of clean Pd-NP and Pd@*um*PPN, respectively and inducing positive charge for Pd corner site on Pd@*um*PPN. The PDOS of Pd corner site is broaden and shifted further from the Fermi-level (E_F) upon interacting with the *um*PPN structure was argued by Yildirim et al. as a characteristic indication for this kind of strong chemisorption enhanced by van der Waals interaction between aromatic rings and transition metals.[98]

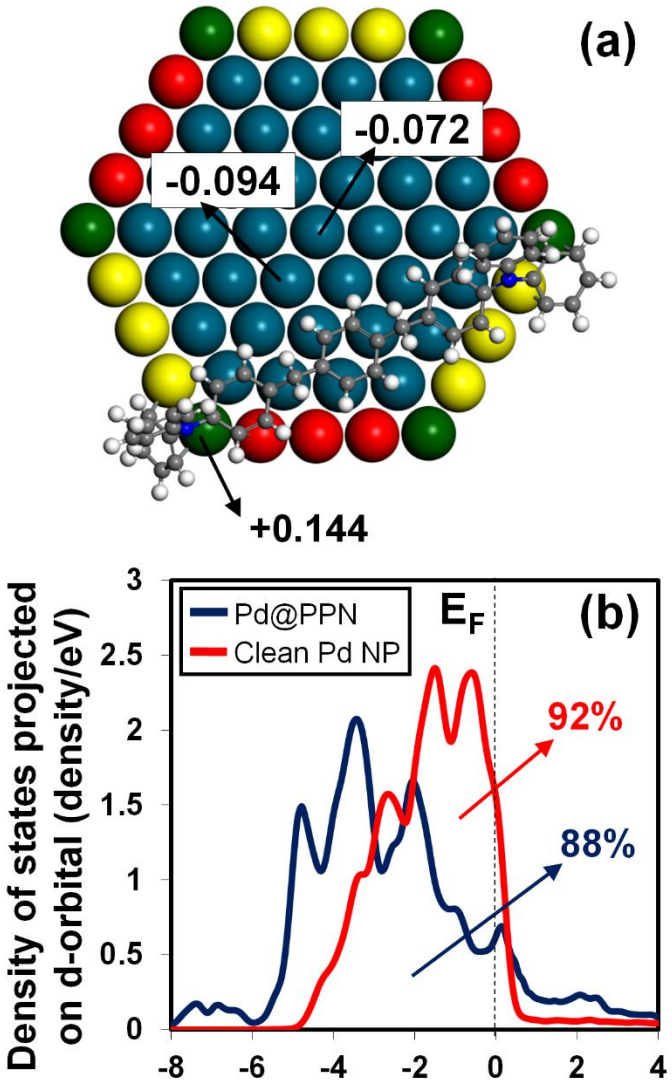

Figure 14: (a) Bader charge of Pd atoms on the Pd_{332} cluster coordinated with adsorbed *um*PPN. (b) Density of states projected on d-orbital (PDOS) for the corner Pd site of Pd_{332}@*um*PPN (blue color) and clean Pd_{332} cluster (red color).

Furthermore, we revealed that there was a net charge of 0.422e$^-$ transferred from the *um*PPN molecule to the Pd-NP, inducing negative charges on Pd atoms in adjacent positions to adsorbed *um*PPN molecule (except the corner site). As seen in Fig. 14a, two Pd atoms next to adsorbed *um*PPN has the charge of -0.094 and -0.072 for the nearer and further atoms, respectively, while the charge of them on the clean Pd-NP is -0.035. Since the charge transfer effect was reported to play very important role in modifying the activity of the catalysts,[97, 99-101] it is likely that the charge transfer from *um*PPN to Pd NP inducing negative charge on Pd atoms could be another factor contributing to the high activity and high selectivity of our fabricated catalyst for the HDO of carboxylic acids. Indeed, the addition of one e$^-$ improved markedly both the reaction kinetics and selectivity of Pd-catalyst for formic acid decomposition was reported recently in Wang et al.[102] More importantly, the negative charge induced on Pd atoms upon the interaction with the polymer frame structure has substantial influence on adsorption and therefore, on reactivity. Besides the rate determining steps that were identified for the DCN/DCX pathways (the C_α-H activations and dehydroxylation reactions), the hydrogenation of hydrocarbons and the removal of strongly bound intermediates such as CO and unsaturated hydrocarbons were also reported as the "bottle-necks" of the HDO conversion.[70, 82] Hydrogenation of unsaturated hydrocarbons was generally considered as surface insensitive reactions,[103-105] so even with high density of step sites in our Pd@PPN catalyst, this reaction is still not much facilitated. On another side, the adsorption energies of all alkene and alkylidyne intermediates are very sensitive to the surface charge of coordinated metal atom, and therefore the charge transfer effect will have greater influence to the kinetic performance of the hydrogenation reaction. Alkylidyne intermediates are bound very strongly on the surface of transition metals and are generally considered as a poison to the catalyst during the hydrogenation.[100, 101, 106] When the charge of surface Pt atom is changed from -0.005 to -0.029, the computed adsorption energies for ethylene and ethylidyne on Pt(111) surface were reduced by 19.2 and 15.4kJ/mol, respectively, consequently increase the hydrogenation rate by an order of magnitude as was reported in Gunasooriya et al.[100] Furthermore, CO binding energy is also weaker on more negative surface atom, although with smaller magnitude than those above-mentioned unsaturated hydrocabons.[99, 100] Therefore due to a net charge transfer from the *um*PPN molecule to the Pd-NP inducing more negative charge of surface Pd atoms makes the removal of the strongly bound intermediates formed during the HDO process become easier and enhance the activity of our fabricated catalyst. It should be noted that when the coverage of *um*PPN is bigger in realistic cases, the charge transfer to Pd NP is then stronger and results in higher promotional effect to the catalytic activity. More insights into the electronic interaction between *um*PPN molecule interacts with smaller Pd_{23} cluster done by Gaussian package via the natural population analysis (NPA) and natural bond orbital (NBO) analysis charge calculations are presented in Tables T4, T5 and T6, SI. Finally, it is important to mention that the interaction and charge transfer between the polymer frame structure and Pd NP is stronger for the smaller Pd NP than for larger particle size. According to our previous study,[66] the 3 nm Pd NP fabricated from the solid-phase hydrogenation procedure (Pd@PPN) was formed anchoring inside the cage of the polymer frame structure and therefore the degree of interaction between the polymer frame structure and Pd NP is maximized. Meanwhile, the 9 nm Pd particle fabricated from the liquid-phase reduction procedure (Pd@PPN-1) was formed anchoring outside the cage of the polymer frame structure and the charge transfer between the polymer frame structure and the Pd-PPN is minimized. That could explain nicely the higher activity of the Pd@PPN catalyst (particle size 3 nm) than the Pd@PPN-1 catalyst (particle size ~9 nm) for the HDO conversion of stearic acid obtained in Table 1 and demonstrate again the importance of charge transfer in facilitating the HDO activity.

Conclusions

In our present investigation, we have designed and developed Pd NPs (2-3 nm size range) encapsulated nitrogen rich porous organic polymer (Pd@PPN) and employed it as robust catalyst towards the conversion of saturated/unsaturated fatty acids to diesel ranged long chain biofuel additive. $FeCl_3$ aided Friedel-Crafts alkylation between triphenylamine (TPA) monomer and α, α'-dibromo-*p*-xylene as cross-linkers successfully furnished self-assembled PPN nanofibers having average length 233-333 nm. This catalyst also exhibited versatile catalytic performance over different types of vegetable oils including palm oil, soyabean oil, sunflower oil and rapeseed oil to furnish long chain diesel range alkanes which definitely established superiority and versatility of Pd@PPN catalyst. It was found from the catalytic details study that decarbonylation route to produce C17 alkane (with one carbon atoms less) is more preferred over the hydrogenation-hydrodehydration route. Our catalyst also shows excellent stability and minimum catalyst leaching after fourth and fifth catalytic run, could be attributed to the strongly bound Pd NPs on highly cross-linked porous organic framework. Two reasons that could explain the good performance of the Pd@PPN catalyst in the HDO of carboxylic acids are revealed. The presence of high density of step sites on the fabricated Pd-NPs anchored in the cage of PPN polymer was predicted from Density Functional Theory (DFT) investigation into the interaction between Pd-NPs and the polymer frame-structure, which promotes the rate-determining steps during the DCN pathway of carboxylic acids and was one of the crucial factors contributing into the high activity of the catalyst. Besides, the charge transfer from the polymer frame structure to the Pd NP induced negative charge of Pd atoms and facilitated the removal of strongly bound intermediates (involving CO and other unsaturated hydrocarbons), which usually acts as poisons to the catalyst during the HDO process, and was identified as another important factor that enhance the stability and activity of the catalyst. Those two factors therefore explain the unprecedented performance of the Pd@PPN catalyst during the Hydrodeoxygenation (HDO) conversion of the long linear chain carboxylic acid to hydrocarbons product and could open up a new efficient way for bio-diesel production.

Conflicts of interest

There are no conflicts to declare.

Acknowledgements

C.S. and S.C.S wish to thankfully acknowledge the Council of Scientific and Industrial Research (CSIR)-University grant commission (UGC), New Delhi, for their respective junior & senior research fellowships. J.M. thanks the Department of Science and Technology, India, for the DST-INSPIRE Faculty Research project grant (GAP-0522) at the CSIR-IICT, Hyderabad and kindly acknowledges CSIR-YSA Research Grant with the reference no: HRDG/YSA-19/02/21(0045)/2019 for the financial support. Q.T.T. and M.P.S. acknowledge the financial support by the Singapore National Research Foundation under its Campus for Research Excellence and Technological Enterprise (CREATE) program through the Cambridge Center for Carbon Reduction in Chemical Technology (C4T) and eCO2EP programs. The computational work for this research is performed with the resources of the National Supercomputing Centre, Singapore (NSCC) under the project ID 12000902. K.A thanks for the support by Basic Science Research Program (2018R1A1A1A05079555) and Technology Development Program to Solve Climate Changes (2017M1A2A2087630) of the National Research Foundation of Korea (NRF) funded by the Ministry of Science and ICT, and MOTIE (KIAT_N0001754) and UNIST (1.180082.01). D.Q.D acknowledges the financial support by Vietnam National Foundation for Science and Technology Development (NAFOSTED) under grant number 103.03-2018.366. N.T.B thanks the support from the National Foundation for Science and Technology Development in the framework of project coded 104.05-2017.39. P.N.A, A.D and F.J. are grateful to the CNRS, the University of Poitiers, the Région Nouvelle Aquitaine for financial support. The International Consortium on Eco-conception and Renewable Resources (FR CNRS INCREASE 3707) and the chair "TECHNOGREEN" are also acknowledged for their funding.

Notes

‡**Supplementary Information:** Characterization description and results. Experimental data: Thermogravimetric analysis (TGA); Fourier transformed infrared (FT-IR) spectra; Pore-size distributions; FE-SEM images; HAADF-STEM images; N1s XPS spectra; Fatty acids compositions of various vegetable oils; TEM images of different Pd-based catalysts; Recycling efficiency testing; HOMO and LUMO distributions; Computational data: Thermodynamics properties, NPA charges and NBO analysis from DFT simulations; Justification on choosing level of theory; Justification on choosing the models; Comparison of adsorptions and reactions on B5 vs F4 step sites; Reactions along RDO pathway on Pd(111) terrace sites and Pd B5 step sites; Other competitive reactions along the DCX and DCN pathways for butanoic acid HDO conversion on Pd(111) terrace sites and Pd B5 step sites; Higher coverage of TPA adsorption on Pd_{322} cluster.

Corresponding authors

qttrinh@ntu.edu.sg; trinhquangthang@duytan.edu.vn (Q.T.T);
mpsherb@berkeley.edu (M.P.S);
johncuchem@gmail.com; johnmondal@iict.res.in (J.M)

References

1. G. W. Huber, S. Iborra and A. Corma, *Chemical Reviews*, 2006, **106**, 4044-4098.

2. Q. T. Trinh, A. Banerjee, Y. Yang and S. H. Mushrif, *The Journal of Physical Chemistry C*, 2017, **121**, 1099-1112.
3. J. J. Varghese, Q. T. Trinh and S. H. Mushrif, *Catalysis Science & Technology*, 2016, **6**, 3984-3996.
4. W. Li, Y. Gao, S. Yao, D. Ma and N. Yan, *Green Chemistry*, 2015, **17**, 4198-4205.
5. P. N. Amaniampong, Q. T. Trinh, K. Li, S. H. Mushrif, Y. Hao and Y. Yang, *Catalysis Today*, 2018, **306**, 172-182.
6. P. N. Amaniampong, Q. T. Trinh, B. Wang, A. Borgna, Y. Yang and S. H. Mushrif, *Angewandte Chemie International Edition*, 2015, **54**, 8928-8933.
7. Q. T. Trinh, B. K. Chethana and S. H. Mushrif, *The Journal of Physical Chemistry C*, 2015, **119**, 17137-17145.
8. P. N. Amaniampong, Q. T. Trinh, K. De Oliveira Vigier, D. Q. Dao, N. H. Tran, Y. Wang, M. P. Sherburne and F. Jérôme, *Journal of the American Chemical Society*, 2019, **141**, 14772-14779.
9. M. Snåre, I. Kubičková, P. Mäki-Arvela, D. Chichova, K. Eränen and D. Y. Murzin, *Fuel*, 2008, **87**, 933-945.
10. R. W. Gosselink, S. A. W. Hollak, S.-W. Chang, J. van Haveren, K. P. de Jong, J. H. Bitter and D. S. van Es, *ChemSusChem*, 2013, **6**, 1576-1594.
11. S. Lestari , P. Mäki-Arvela, J. Beltramini, G. Q. M. Lu and D. Y. Murzin, *ChemSusChem*, 2009, **2**, 1109-1119.
12. C. Zhao, T. Brück and J. A. Lercher, *Green Chemistry*, 2013, **15**, 1720-1739.
13. J. Dupont, P. A. Z. Suarez, M. R. Meneghetti and S. M. P. Meneghetti, *Energy & Environmental Science*, 2009, **2**, 1258-1265.
14. T. Sooknoi, T. Danuthai, L. L. Lobban, R. G. Mallinson and D. E. Resasco, *Journal of Catalysis*, 2008, **258**, 199-209.
15. N. Taufiqurrahmi and S. Bhatia, *Energy & Environmental Science*, 2011, **4**, 1087-1112.
16. G. W. Huber, P. O'Connor and A. Corma, *Applied Catalysis A: General*, 2007, **329**, 120-129.
17. A. Srivastava and R. Prasad, *Renewable and Sustainable Energy Reviews*, 2000, **4**, 111-133.
18. S. N. Naik, V. V. Goud, P. K. Rout and A. K. Dalai, *Renewable and Sustainable Energy Reviews*, 2010, **14**, 578-597.
19. E. Santillan-Jimenez and M. Crocker, *Journal of Chemical Technology & Biotechnology*, 2012, **87**, 1041-1050.
20. S. H. Mushrif, V. Vasudevan, C. B. Krishnamurthy and B. Venkatesh, *Chemical Engineering Science*, 2015, **121**, 217-235.
21. M. M. K. Bhuiya, M. G. Rasul, M. M. K. Khan, N. Ashwath, A. K. Azad and M. A. Hazrat, *Renewable and Sustainable Energy Reviews*, 2016, **55**, 1129-1146.
22. T. Kalnes, T. Marker and R. Shonnard David, *Journal*, 2007, **5**.
23. P. N. Amaniampong, Q. T. Trinh, J. J. Varghese, R. Behling, S. Valange, S. H. Mushrif and F. Jérôme, *Green Chemistry*, 2018, **20**, 2730-2741.
24. S. De, B. Saha and R. Luque, *Bioresource Technology*, 2015, **178**, 108-118.
25. A. E. Atabani, A. S. Silitonga, H. C. Ong, T. M. I. Mahlia, H. H. Masjuki, I. A. Badruddin and H. Fayaz, *Renewable and Sustainable Energy Reviews*, 2013, **18**, 211-245.
26. D. Kim, D. R. Vardon, D. Murali, B. K. Sharma and T. J. Strathmann, *ACS Sustainable Chemistry & Engineering*, 2016, **4**, 1775-1784.
27. M. Hajjari, M. Tabatabaei, M. Aghbashlo and H. Ghanavati, *Renewable and Sustainable Energy Reviews*, 2017, **72**, 445-464.
28. S. Liu, T. Simonetti, W. Zheng and B. Saha, *ChemSusChem*, 2018, **11**, 1446-1454.
29. S. Mondal, R. Singuru, S. Chandra Shit, T. Hayashi, S. Irle, Y. Hijikata, J. Mondal and A. Bhaumik, *ACS Sustainable Chemistry & Engineering*, 2018, **6**, 1610-1619.
30. G. Xu, Y. Zhang, Y. Fu and Q. Guo, *ACS Catalysis*, 2017, **7**, 1158-1169.
31. J. Chen and Q. Xu, *Catalysis Science & Technology*, 2016, **6**, 7239-7251.
32. H. Zhang, H. Lin, W. Wang, Y. Zheng and P. Hu, *Applied Catalysis B: Environmental*, 2014, **150-151**, 238-248.
33. J. Zhang and C. Zhao, *ACS Catalysis*, 2016, **6**, 4512-4525.
34. Y. Zhang and S. N. Riduan, *Chemical Society Reviews*, 2012, **41**, 2083-2094.
35. S. Mondal, S. K. Kundu and A. Bhaumik, *Chemical Communications*, 2017, **53**, 2752-2755.
36. R. Gomes, P. Bhanja and A. Bhaumik, *Chemical Communications*, 2015, **51**, 10050-10053.
37. R. Dawson, A. I. Cooper and D. J. Adams, *Progress in Polymer Science*, 2012, **37**, 530-563.
38. X. Zou, H. Ren and G. Zhu, *Chemical Communications*, 2013, **49**, 3925-3936.
39. M. Nihei, H. Ida, T. Nibe, A. M. P. Moeljadi, Q. T. Trinh, H. Hirao, M. Ishizaki, M. Kurihara, T. Shiga and H. Oshio, *Journal of the American Chemical Society*, 2018, **140**, 17753-17759.
40. V. M. Suresh, S. Bonakala, H. S. Atreya, S. Balasubramanian and T. K. Maji, *ACS Applied Materials & Interfaces*, 2014, **6**, 4630-4637.
41. Q. Fang, S. Gu, J. Zheng, Z. Zhuang, S. Qiu and Y. Yan, *Angewandte Chemie International Edition*, 2014, **53**, 2878-2882.
42. K. Dhanalaxmi, R. Singuru, S. Mondal, L. Bai, B. M. Reddy, A. Bhaumik and J. Mondal, *ACS Sustainable Chemistry & Engineering*, 2017, **5**, 1033-1045.
43. R. Singuru, K. Dhanalaxmi, S. C. Shit, B. M. Reddy and J. Mondal, *ChemCatChem*, 2017, **9**, 2550-2564.
44. S. Mondal, B. C. Patra and A. Bhaumik, *ChemCatChem*, 2017, **9**, 1469-1475.
45. P. Munnik, P. E. de Jongh and K. P. de Jong, *Chemical Reviews*, 2015, **115**, 6687-6718.
46. G. Kresse and J. Hafner, *Physical Review B*, 1993, **47**, 558-561.
47. G. Kresse and J. Furthmüller, *Computational Materials Science*, 1996, **6**, 15-50.
48. P. E. Blöchl, *Physical Review B*, 1994, **50**, 17953-17979.
49. J. Klimeš, D. R. Bowler and A. Michaelides, *Journal of Physics: Condensed Matter*, 2009, **22**, 022201.
50. J. Klimeš, D. R. Bowler and A. Michaelides, *Physical Review B*, 2011, **83**, 195131.
51. O. Mohan, Q. T. Trinh, A. Banerjee and S. H. Mushrif, *Molecular Simulation*, 2019, **45**, 1163-1172.
52. Q. T. Trinh, A. V. Nguyen, D. C. Huynh, T. H. Pham and S. H. Mushrif, *Catalysis Science & Technology*, 2016, **6**, 5871-5883.
53. H. Yildirim, T. Greber and A. Kara, *The Journal of Physical Chemistry C*, 2013, **117**, 20572-20583.
54. J. Carrasco, W. Liu, A. Michaelides and A. Tkatchenko, *The Journal of Chemical Physics*, 2014, **140**, 084704.
55. S. E. M. Putra, F. Muttaqien, Y. Hamamoto, K. Inagaki, I. Hamada and Y. Morikawa, *The Journal of Chemical Physics*, 2019, **150**, 154707.
56. C. T. Campbell, *Accounts of Chemical Research*, 2019, **52**, 984-993.
57. G. Henkelman, B. P. Uberuaga and H. Jónsson, *The Journal of Chemical Physics*, 2000, **113**, 9901-9904.

58. K. Honkala, A. Hellman, I. N. Remediakis, A. Logadottir, A. Carlsson, S. Dahl, C. H. Christensen and J. K. Nørskov, *Science*, 2005, **307**, 555-558.
59. Y.-H. Chin, C. Buda, M. Neurock and E. Iglesia, *Journal of the American Chemical Society*, 2013, **135**, 15425-15442.
60. Y.-H. Chin, C. Buda, M. Neurock and E. Iglesia, *Journal of the American Chemical Society*, 2011, **133**, 15958-15978.
61. I. V. Yudanov, A. Genest, S. Schauermann, H.-J. Freund and N. Rösch, *Nano Letters*, 2012, **12**, 2134-2139.
62. B. T. Loveless, C. Buda, M. Neurock and E. Iglesia, *Journal of the American Chemical Society*, 2013, **135**, 6107-6121.
63. L. Zhou, J. M. P. Martirez, J. Finzel, C. Zhang, D. F. Swearer, S. Tian, H. Robatjazi, M. Lou, L. Dong, L. Henderson, P. Christopher, E. A. Carter, P. Nordlander and N. J. Halas, *Nature Energy*, 2020, **5**, 61-70.
64. W. Tang, E. Sanville and G. Henkelman, *Journal of Physics: Condensed Matter*, 2009, **21**, 084204.
65. G. Henkelman, A. Arnaldsson and H. Jónsson, *Computational Materials Science*, 2006, **36**, 354-360.
66. J. Mondal, Q. T. Trinh, A. Jana, W. K. H. Ng, P. Borah, H. Hirao and Y. Zhao, *ACS Applied Materials & Interfaces*, 2016, **8**, 15307-15319.
67. M. Hacene, A. Anciaux-Sedrakian, X. Rozanska, D. Klahr, T. Guignon and P. Fleurat-Lessard, *Journal of Computational Chemistry*, 2012, **33**, 2581-2589.
68. M. Hutchinson and M. Widom, *Computer Physics Communications*, 2012, **183**, 1422-1426.
69. S. Maintz, B. Eck and R. Dronskowski, *Computer Physics Communications*, 2011, **182**, 1421-1427.
70. J. Lu, S. Behtash and A. Heyden, *The Journal of Physical Chemistry C*, 2012, **116**, 14328-14341.
71. A. Banerjee, A. P. van Bavel, H. P. C. E. Kuipers and M. Saeys, *ACS Catalysis*, 2015, **5**, 4756-4760.
72. A. Banerjee, A. P. van Bavel, H. P. C. E. Kuipers and M. Saeys, *ACS Catalysis*, 2017, **7**, 5289-5293.
73. J. Xu and M. Saeys, *The Journal of Physical Chemistry C*, 2009, **113**, 4099-4106.
74. C. Sarkar, S. Pendem, A. Shrotri, D. Q. Dao, P. Pham Thi Mai, T. Nguyen Ngoc, D. R. Chandaka, T. V. Rao, Q. T. Trinh, M. P. Sherburne and J. Mondal, *ACS Applied Materials & Interfaces*, 2019, **11**, 11722-11735.
75. R. Singuru, Q. T. Trinh, B. Banerjee, B. Govinda Rao, L. Bai, A. Bhaumik, B. M. Reddy, H. Hirao and J. Mondal, *ACS Omega*, 2016, **1**, 1121-1138.
76. Q. T. Trinh, J. Yang, J. Y. Lee and M. Saeys, *Journal of Catalysis*, 2012, **291**, 26-35.
77. L. Li, H. Zhao, J. Wang and R. Wang, *ACS Nano*, 2014, **8**, 5352-5364.
78. H. Zhong, C. Liu, H. Zhou, Y. Wang and R. Wang, *Chemistry – A European Journal*, 2016, **22**, 12533-12541.
79. P. Puthiaraj and K. Pitchumani, *Green Chemistry*, 2014, **16**, 4223-4233.
80. S. Mondal, J. Mondal and A. Bhaumik, *ChemCatChem*, 2015, **7**, 3570-3578.
81. H. Zhong, C. Liu, Y. Wang, R. Wang and M. Hong, *Chemical Science*, 2016, **7**, 2188-2194.
82. J. Lu, S. Behtash, M. Faheem and A. Heyden, *Journal of Catalysis*, 2013, **305**, 56-66.
83. Y. K. Lugo-José, S. Behtash, M. Nicholson, J. R. Monnier, A. Heyden and C. T. Williams, *Journal of Molecular Catalysis A: Chemical*, 2015, **406**, 85-93.
84. A. Srifa, K. Faungnawakij, V. Itthibenchapong and S. Assabumrungrat, *Chemical Engineering Journal*, 2015, **278**, 249-258.
85. S. Akbayrak and S. Özkar, *ACS Applied Materials & Interfaces*, 2012, **4**, 6302-6310.
86. S. Lestari, P. Mäki-Arvela, H. Bernas, O. Simakova, R. Sjöholm, J. Beltramini, G. Q. M. Lu, J. Myllyoja, I. Simakova and D. Y. Murzin, *Energy & Fuels*, 2009, **23**, 3842-3845.
87. R. Arrigo, M. E. Schuster, Z. Xie, Y. Yi, G. Wowsnick, L. L. Sun, K. E. Hermann, M. Friedrich, P. Kast, M. Hävecker, A. Knop-Gericke and R. Schlögl, *ACS Catalysis*, 2015, **5**, 2740-2753.
88. I. L. Simakova, O. A. Simakova, A. V. Romanenko and D. Y. Murzin, *Industrial & Engineering Chemistry Research*, 2008, **47**, 7219-7225.
89. S. Lestari, P. Mäki-Arvela, I. Simakova, J. Beltramini, G. Q. M. Lu and D. Y. Murzin, *Catalysis Letters*, 2009, **130**, 48-51.
90. J. P. Ford, J. G. Immer and H. H. Lamb, *Topics in Catalysis*, 2012, **55**, 175-184.
91. L. Boda, G. Onyestyák, H. Solt, F. Lónyi, J. Valyon and A. Thernesz, *Applied Catalysis A: General*, 2010, **374**, 158-169.
92. W. Jin, L. Pastor-Pérez, D. Shen, A. Sepúlveda-Escribano, S. Gu and T. Ramirez Reina, *ChemCatChem*, 2019, **11**, 924-960.
93. S. Kim, E. E. Kwon, Y. T. Kim, S. Jung, H. J. Kim, G. W. Huber and J. Lee, *Green Chemistry*, 2019, **21**, 3715-3743.
94. Q. Bu, H. Lei, A. H. Zacher, L. Wang, S. Ren, J. Liang, Y. Wei, Y. Liu, J. Tang, Q. Zhang and R. Ruan, *Bioresource Technology*, 2012, **124**, 470-477.
95. G. T. K. K. Gunasooriya, A. P. van Bavel, H. P. C. E. Kuipers and M. Saeys, *ACS Catalysis*, 2016, **6**, 3660-3664.
96. Q. T. Trinh, K. F. Tan, A. Borgna and M. Saeys, *The Journal of Physical Chemistry C*, 2013, **117**, 1684-1691.
97. Y. Lykhach, S. M. Kozlov, T. Skála, A. Tovt, V. Stetsovych, N. Tsud, F. Dvořák, V. Johánek, A. Neitzel, J. Mysliveček, S. Fabris, V. Matolín, K. M. Neyman and J. Libuda, *Nature Materials*, 2016, **15**, 284-288.
98. H. Yildirim and A. Kara, *The Journal of Physical Chemistry C*, 2013, **117**, 2893-2902.
99. Y. P. G. Chua, G. T. K. K. Gunasooriya, M. Saeys and E. G. Seebauer, *Journal of Catalysis*, 2014, **311**, 306-313.
100. G. T. K. K. Gunasooriya, E. G. Seebauer and M. Saeys, *ACS Catalysis*, 2017, **7**, 1966-1970.
101. A. S. Crampton, M. D. Rötzer, C. J. Ridge, F. F. Schweinberger, U. Heiz, B. Yoon and U. Landman, *Nature Communications*, 2016, **7**, 10389.
102. P. Wang, S. N. Steinmann, G. Fu, C. Michel and P. Sautet, *ACS Catalysis*, 2017, **7**, 1955-1959.
103. R. A. Van Santen, *Accounts of Chemical Research*, 2009, **42**, 57-66.
104. C.-K. Tsung, J. N. Kuhn, W. Huang, C. Aliaga, L.-I. Hung, G. A. Somorjai and P. Yang, *Journal of the American Chemical Society*, 2009, **131**, 5816-5822.
105. R. Pestman, W. Chen and E. Hensen, *ACS Catalysis*, 2019, **9**, 4189-4195.
106. P. S. Cremer, X. Su, Y. R. Shen and G. A. Somorjai, *Journal of the American Chemical Society*, 1996, **118**, 2942-2949.

ARTICLE

Table of Contents: Graphical Abstract

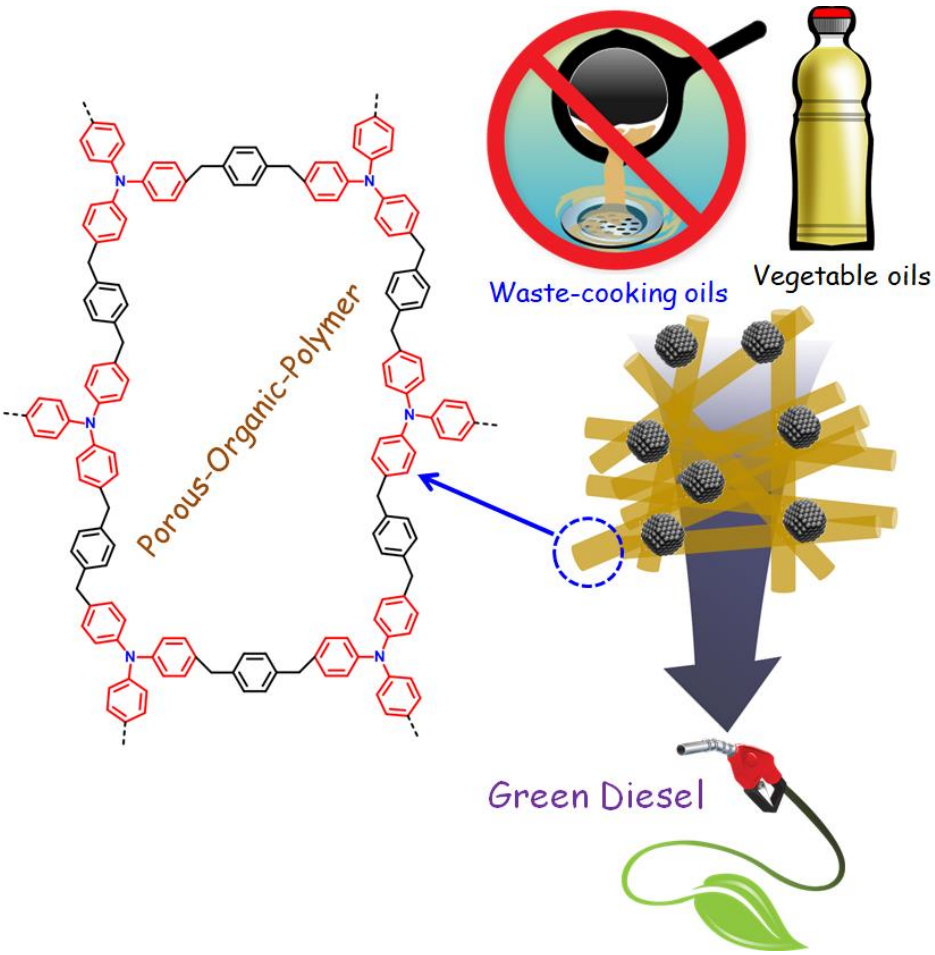

Abstract: Novel design Pd-based catalyst hosted over nitrogen enriched fibrous Porous-Organic-Polymer exposes a high density of step sites and exhibits versatile catalytic performance over different types of vegetable oils to furnish long chain diesel-range alkanes.